Master Thesis

Microscopic Theory of the Overlayer Plasmon on Si(100) 2×1-K Surface.

by

Hiroshi Ishida

Department of Physics,

Faculty of Science,

University of Tokyo.

January 1985

Microscopic Theory of the Overlayer Plasmon

on Si(100) 2×1-K Surface

Contents

1. Introduction 1

2. Microscopic Picture of Overlayer Plasmon 3

3. Structure and Electronic Properties of
Alkali Overlayers on Si(100) 2×1 Surface 8

4. Parallel Rod Model 13

5. Electronic Structure of Si(100) 2×1-K Surface . . . 27

6. Dispersion of the Overlayer Plasmon
based on the Surface Band Calculation 37

7. Conclusion and Discussion 57

Acknoledgement 60

References 61

Figure Captions 63

Figures and Tables 66

1. Introduction

Overlayer plasmon is a collective excitation of electrons whose charge fluctuation is localized in a metal monolayer adsorbed on the surface of other materials. Its dispersion, i.e., plasmon energy v.s. 2-dimensional wavevector, is quite sensitive to the microscopic structure of surface and thus can be a powerful tool to analyze metal overlayer systems. Supported by the steady developments of the ultra high vacuum technology and various experimental techniques to study surface, it has now become possible to measure the overlayer plasmon dispersion of clean surface with high resolution. Recently Aruga, Tochihara and Murata have investigated the overlayer plasmon on Si(100) 2×1-K surface extensively.[1] The measured dispersion depends on the direction of the wavevector, which suggests a strong anisotropy of the surface structure. Then it has become important to examine theoretically whether the structure model proposed based on the previous experiments is able to reproduce the observed plasmon dispersion.

Accompanied by the rapid progress of computers, methods of the band calculation of surface are advanced these days nearly to the level of exact science and the reconstruction of surface structure is now investigated through the surface band structure calculated with them. On the other hand, almost all of the theories of overlayer plasmon advanced so far are phenomenological[2~5] and there is no theoretical work on overlayer plasmon that takes account of a realistic electronic structure of a particular surface. Although phenomenological theories are surely useful to make

clear some qualitative aspects of overlayer plasmon, the gap between them and the elaborate band theories seems too large to be left as it is.

In this master thesis, we calculate the dispersion of the overlayer plasmon on Si(100) 2×1-K surface non-empirically based on the self-consistent band calculation and discuss the validity of the structure model through the comparison between the theory and the experiment. At the same time we shall elucidate the qualitative features of the overlayer plasmon of alkali overlayers on Si(100) 2×1 surface using a model which is simple, but still, quantum mechanical.

The plan of this master thesis is as follows. As the term "overlayer plasmon" does not seem well-known, we explain the microscopic picture of overlayer plasmon in section 2. In section 3, experimental works on the alkali overlayers on Si(100) surface, such as the structure model of the overlayer and the observed plasmon dispersion, are reviewed. In section 4, we introduce a simplified model which simulates alkali overlayers on Si(100) surface and clarify the features of overlayer plasmon in such systems. Section 5 and section 6 are devoted to the fully microscopic theory of the overlayer plasmon. In section 5, we reveal the surface band structure of Si(100) 2×1-K surface with the self-consistent LCAO-X_α method. Based on this band calculation, the dispersion of the overlayer plasmon is calculated non-empirically in section 6. Finally, conclusion and discussion are given in section 7.

Throughout this master thesis, we use atomic unit and thus Plank constant $\hbar$ and the unit charge e are set equal to unity.

2. Microscopic Picture of Overlayer Plasmon

There appear several kinds of plasmons in solid state physics. Among them, overlayer plasmon is not very popular and the number of the literature which reports its observation is very small. As stated in the introduction, overlayer plasmon is a normal mode of charge fluctuation localized in a metal monolayer adsorbed on the surface of other materials. The investigations of metal adatom layers on surface have been continued extensively. For instance, it is known that the reconstruction of Si surface changes variedly by the adsorption of transition metals.[6~7] In connection with plasmon modes, it is revealed that the dispersion of the surface plasmon (not overlayer plasmon) of Si or Ge is affected by the adatom layers of transition metals such as Au, Ag.[8] However, in the adatom layers of such noble metals, overlayer plasmon has never been observed and all the overlayer plasmons observed so far are those excited in the alkali metal overlayers adsorbed on Si[1,26~27] and on several transition metals such as Ni, Cu, W.[9~12] Thus it is expected that existence of the overlayer plasmon crucially depends on the electronic structure of the adatom layer.

Adsorption of alkali atoms on solid surfaces has been intensively studied as an example of simple chemisorption system. In contrast to the cases of transition metals, covalent interaction between alkali atoms and the substrate is not so strong and alkali atoms do not have a much influence on the cofiguration of the substrate. At the full coverage alkali atoms form an ordered monolayer on the

substrate surface and delocalized surface bands are formed in the overlayer. The valence electrons of alkali atoms are accomodated in them and the alkali overlayer becomes metallic. (see section 3)

Excitations of valence electrons within a single or between two surface bands are the origin of the overlayer plasmon and in fact all the microscopic theories of the overlayer plasmon proposed so far are based on this view.[14,28,31] Then overlayer plasmon is classified into two groups according to the character of single particle excitations from which the plasmon is made. If the single particle excitations between two different surface bands become a collective excitation, it is called inter-surface-band plasmon. On the other hand, if the single particle excitations in a partially occupied surface band become the collective, such a mode is called as intra-surface-band plasmon. The latter mode is characteristic of a metallic overlayer while the former one can exist even if the overlayer is insulative. Overlayer plasmon once attracted a great deal of attention as an evidence of Mott transition in the metal overlayer.[10] But direct connection was later discarded because of the existence of intersurfaceband modes.

Here the difference between the overlayer plasmon and the surface plasmon should be remarked. Surface plasmon was first predicted by Ritchie using a simple dielectric model in 1957[13]. As is well known, its frequency is roughly given by $\omega_p/2^{1/2}$ with bulk plasmon frequency ω_p. Overlayer plasmon and surface plasmon have the common features that charge fluctuation due to them is localized in the surface

region and that both plasmon dispersions are very sensitive to the structure of the surface. However, the character of single particle excitations from which the plasmon is made is quite different between overlayer plasmon and surface plasmon. As explained above, we think overlayer plasmon is a collective excitation of electrons between surface bands. On the other hand, surface plasmon is regarded as a collective excitation in bulk states though it reflects wave functions of bulk states in the surface region. However, it should be noted that energy of overlayer plasmon converges to that of surface plasmon as the thickness of the overlayer becomes large and as surface bands in the overlayer come to have bulklike characters.

To make the microscopic picture of overlayer plasmon clearer, we introduce Newns' box model[14] here, which is the only one microscopic model of alkali overlayers presented thus far. In this model electrons of alkali overlayers are confined in an uniform thin film with thickness l as shown in Fig. 2. 1. The substrate is modeled by the semi-infinite dielectric medium with a dielectric constant $\varkappa$. The eigenfunction and the energy of electrons are then written as

$$\phi_{k,p}(r) = \frac{1}{L} e^{i\vec{k}\cdot\vec{x}} \sqrt{\frac{2}{l}} \sin\left(\frac{p\pi}{l} z\right) \qquad (2.1)$$

$$\epsilon_{k\,p} = \frac{1}{2m} k^2 + \frac{1}{2\mu}\left(\frac{p\pi}{l}\right)^2 \quad , \qquad (2.2)$$

where m and μ are the parallel and normal electron mass and integer p-1 means the number of nodes of the wave function in z-direction. Newns considered the lowest two modes p=1, 2

which approximately correspond to s, p_z valence orbitals of (a) alkali atom. The lower band ε_k^1 is assumed partially occupied while the higher one ε_k^2 is assumed empty. Then as shown in Fig. 2.2, following two excitation modes are possible; (A) s-s intraband plasmon mode (B) s-p_z interband plasmon mode. With the RPA equation (see section 4), Newns derived the plasmon dispersion of these modes as follows;

(A)-mode (s-s intraband mode)

$$\omega^2(\vec{Q}) = \frac{k_f^2}{m} Q \left\{ \frac{2}{K+1} + \left(\frac{5}{4\pi^2} - \frac{1}{3} + \frac{K-1}{K+1} \ell Q \right) \right\} \quad . \quad (2.3)$$

The plasmon energy is proportional to $Q^{1/2}$ in small Q regions and the polarization field is parallel to the surface. This mode is called 2-dimensional plasmon and is observed in the system of electrons trapped at the surface of liquid He.

(B)-mode (s-p_z interband mode)

$$\omega^2(\vec{Q}) = \left(\frac{3\pi^2}{2M\ell^2} \right)^2 + \frac{6\pi^2 k_f^2}{2M\ell^2} \left\{ \frac{10\ell}{9\pi^2} - \frac{2K}{K+1} \left(\frac{16\ell}{9\pi^2} \right)^2 Q \right\} \quad (2.4)$$

The polarization field of this mode is perpendicular to the surface. The plasmon energy is finite at Q=0 and depends negative linearly on Q in small Q regions. Similar mode is also found by Gadzuk[2] and by Ferrel[15] using a simple dielectric model.

In this section we considered the overlayer plasmon as a collective excitation of electrons between surface bands formed in the overlayer and this picture will be retained through this master thesis. In fact, such a picture must be the best one for the alkali overlayer on semiconductor

surfaces with which we will be concerned. Overlayer plasmons have been also observed on the alkali monolayer on transition metals. We consider the the similar mechanism may hold here as in the case of alkali systems on semiconductor surfaces. However, it is not certain since, at the present stage, we do not know what kind of surface bands are involved in the plasmons of the alkali overlayer on metal systems.

3. Structure and Electronic Properties of Alkali Overlayer on Si(100) 2×1 Surface

Alkali overlayers on Si(100) surface show various interesting properties which are important from both fundamental and technological view points. As will be revealed in the following, these properties have a close relation with the peculiar microscopic structure of the alkali overlayers.

When a Si(100) surface is clean, it has a 2×1 reconstruction. Various models are advanced to explain this structure, but the symmetric dimer model proposed by Schleer and Farnworth[16] was most widely accepted as a rough sketch of the surface structure. In this model, two neighboring surface atoms are assumed to make a pair to reduce the number of dangling bonds as illustrated in Fig. 3.1a and 3.1b. Later this model was refined to the asymmetric dimer model shown in Fig. 3.1c. Its evidences were provided by LEED[17], He diffraction measurement[18], ion scattering spectroscopy[19] and ARUPS[20], and theoretical energy minimization also confirmed that the asymmetric dimer is more stable than the symmetric one[21]. The asymmetric dimer model is now regarded as the most reliable structure model for the clean Si(100) surface.

Systematic investigations of alkali overlayers on Si(100) were initiated in regard to negative electron affinity (NEA). NEA is achieved when the work function is reduced so much that the bulk conduction band bottom is raised higher than the vacuum level. With NEA, electrons thermalized into the conduction band can be easily diffused into vacuum,

hence such a surface can be utilized as a highly efficient electron emitter. Among the crystal surfaces of Si, the (100) surface is the only one that can be activated to NEA by the adsorption of the monolayer of alkali atoms (mainly Cs) followed by the oxygen atom chemisorption.[22] Since the formation of the dipole layer due to the charge transfer from alkali atoms to oxygen atoms is the main cause for the decrease of the work function, this fact implies that the adsorption sites of alkali and oxygen atoms on Si(100) surface are particularly fitted to make a large dipole.

Goldstein was the first to study extensively the adsorption of Cs and O on Si(100) surface.[23] The Cs overlayer was found to show a clear 2×1 LEED pattern, whose intensities were different from those of the clean Si(100) surface. Based on this experiment and the symmetric dimer model, Levine[24] proposed a structure model for the Si(100) 2×1-Cs surface shown in Fig. 3.2. In his model, alkali atoms sit on the four fold hollow site between the two symmetric dimers and form raised rows of 1-dimensional chains which extend along the (1,1,0) direction. When oxygenation is carried out on this surface, oxygen atoms must be located in the large caves between the raised rows of Cs chains. Therefore the large dipole between Cs and O which significantly reduces the work function is expected for this model. Later Holtom and Gundry examined the coverage dependence of the structure of alkali overlayers by LEED observation and proposed that alkali atoms can also sit on the bridge site on a dimer.[25]

As stated above, the asymmetric dimer is found slightly more stable than the symmetric one for the clean Si(100)

surface. However, it is not certain whether Levine's model require some rectifications regarding the asymmetric distortion of the substrate dimers since the relative stability of the asymmetric v.s. symmetric dimer changes by the interaction with the alkali adatoms. Anyhow it has been established from LEED observation that alkali atoms form 1-dimensional chains on Si(100) 2×1 surface. Moreover it must be preferable that these chains are located on the raised sites of substrate Si than are submerged in the substrate in order to achieve NEA. More minute differences of the structure would not be essential.

One of the particularly interesting phenomena involved with the alkali overlayer on Si(100) surface is the insulator-metal transition of the overlayer, which was extensively studied by Tochihara.[26~27] In low coverages alkali atoms are adsorbed randomly along the rows of raised sites of the substrate Si and valence electrons of alkali adatoms are transferred into the substrate. This was verified by the rapid decrease of the work function (3~4(eV)) and the core level shift of the alkali atom. With increasing coverage the distance between neighboring adatoms becomes shorter and delocalized surface bands are formed. Then the valence electrons of alkali atoms begin to return to the alkali overlayer and beyond a certain coverage the overlayer changes from insulative to metallic. In the metallic regime, the work function increases slowly until it reaches the saturation value at the full coverage and the core level shift of the alkali atom is also saturated. However, the onset of the plasmon peak in the electron energy loss spectrum is the most conspicuous evidence to

show the appearance of the metallic alkali overlayer. This peak grows very rapidly with increasing coverage and is obviously distinguished from the loss peak of single particle excitations. The observed plasmon energy was found almost constant regardless of the coverages, which was in contrast to the cases of alkali overlayers on transition metals[9~12], where plasmon energy becomes larger with increasing coverages on account of the increase of electron density in the overlayer. This was interpreted by Tochihara[27] based on the structure model presented above as follows; for the alkali overlayer on Si(100) surface, the effective electron density is independent of the coverage in the metallic regime and only the length of the metallic chains is affected by the coverage.

Recently Aruga, Tochihara and Murata have exhaustively investigated the dispersion of the overlayer plasmon of Si(100) 2×1-K surface at the full coverage by AREELS (angle resolved electron energy loss spectroscopy).[1] The measured plasmon dispersion is shown in Fig. 3.3. Here it can not be determined experimentally which of the two azimuth ((1,-1,0) or (1,1,0)) the plasmon dispersion in the left half of the figure corresponds to, since the Si(100) 2×1-K surface is composed of two kinds of domain structures. The plasmon energy corresponding to the main loss peak has a finite energy (~1.7(eV)) in the limit of 2-dimensional wave vector Q=0 and its dispersion depends positive linearly on Q in small Q regions. (In the energy loss spectrum of the (1,0,0) azimuth they also found a shoulder on the lower tail of the main loss peak, which may be assigned to another excitation mode.) As can be seen from the figure, the slope

of the observed plasmon dispersion in small Q regions clearly shows an azimuth dependent anisotropy. This is again considered to reflect the peculiar "chain" structure of the alkali overlayer.

4. Parallel Rod Model[28)]

A. Model

As explained in sec. 3, the alkali overlayer forms a peculiar chain structure on Si(100) 2×1 surface. The observed plasmon energy corresponding to the main loss peak has a finite energy at Q=0, and the dispersion has a positive linear slope in small Q regions. These behaviours are not understood with the uniform Newns' model in section 2. To elucidate the characteristic features of the overlayer plasmon in such a system, we introduce a simplified parallel rod model in this section. As depicted in Fig. 4. 1, the model consists of rectangular rods confining free electrons. The rods have side lengths l_1, l_2 and are arrayed in parallel at intervals of a on the uniform substrate surface.

The eigenfunction and the energy of electrons confined in the n-th rod can be written as

$$\phi_{\substack{pq \\ kn}}(\pi) = \frac{2}{\sqrt{l_1 l_2 L}} e^{iky} \sin\left(\frac{p\pi}{l_1}(x - na)\right) \sin\left(\frac{q\pi}{l_2} z\right) \qquad (4.1)$$

and

$$\epsilon_{\substack{pq \\ k}} = \frac{k^2}{2m} + \frac{1}{2\mu_1}\left(\frac{p\pi}{l_1}\right)^2 + \frac{1}{2\mu_2}\left(\frac{q\pi}{l_2}\right)^2, \qquad (4.2)$$

where m is the free electron mass and μ_1, μ_2 are the effective masses for x, z directions, respectively. The integers p-1 and q-1 mean the number of nodes of the wave function in x and z direction, respectively. Thus the modes

$(p,q)=(1,1),(1,2),(2,1)$ approximately correspond to K-$4s, 4p_z, 4p_x$ orbitals. For the sake of simplicity, the substrate of Si is modeled by the uniform semi-infinite dielectric medium with a dielectric constant $\varkappa$.

B. The RPA equation and its Application to the Model

First, let us derive the RPA equation which is the basis for microscopic theories of the overlayer plasmon. Consider induced charge $\rho_{ind}(r,\omega)$ in the system due to external charge $\rho_{ext}(r,\omega)$. By the linear response theory, it is given by

$$\rho_{ind}(\xi,\omega) = \chi(\xi,\xi_1,\omega)\, G(\xi_1,\xi_2)\, \rho_{ext}(\xi_2,\omega) \quad (4.3)$$

as illustrated in Fig. 4.2a. Here each ξ stands for a set of position and spin coordinates (r,σ), and the repeated letters ξ_1, ξ_2 are understood to indicate appropriate integration and summation. $G(\xi_1,\xi_2)$ is the interaction potential between two unit charges, and $\chi(\xi_1,\xi_2,\omega)$ is the density response function defined as

$$\chi(\xi_1,\xi_2,\omega) = \frac{1}{2\pi i}\int_0^\infty dt\, e^{i(\omega+i\delta)t} \times \left\langle \left[\psi^+(\xi_1,t)\psi(\xi_1,t),\ \psi^+(\xi_2,0)\psi(\xi_2,0) \right] \right\rangle . \quad (4.4)$$

In the RPA, $\chi(\xi_1,\xi_2,\omega)$ is approximated as follows:

$$\chi(\xi_1,\xi_2,\omega) = \chi_0(\xi_1,\xi_2,\omega) + \chi_0(\xi_1,\xi_3,\omega)\, G(\xi_3,\xi_4)\, \chi(\xi_4,\xi_2,\omega) , \quad (4.5)$$

where $\chi_0(\xi_1,\xi_2,\omega)$ is expressed by the simplest graph

made of the product of two one-particle Green's functions as shown in Fig. 4.2b. In this approximation the electron-hole attraction terms which lead to "exciton" mode are neglected. But "plasmon" mode with which we are concerned with would not be affected very much by such a short range screened interaction. By inserting eq. (4.5) into eq. (4.3), we obtain

$$\rho_{ind}(\xi,\omega) = \chi_0(\xi,\xi_1,\omega)\, G(\xi_1,\xi_2) \times \left\{ \rho_{ind}(\xi_2,\omega) + \rho_{ext}(\xi_2,\omega) \right\}, \quad (4.6)$$

(refer Fig. 4.2c)

which means electrons response to the Hartree field of the total charge fluctuation. The response function $\chi_0(\xi_1, \xi_2, \omega)$ in eq. (4.6) can be written using the energy and the wavefunction of approximate one electron states as follows;

$$\chi_0(\xi_1,\xi_2,\omega) = \sum_{i,j} \frac{f_i - f_j}{\epsilon_i - \epsilon_j + \omega + i\delta} \phi_i^*(\pi_1)\phi_j(\pi_1)\phi_i(\pi_2)\phi_j^*(\pi_2) \qquad (\sigma_1 = \sigma_2)$$

$$= 0 \qquad (\sigma_1 \neq \sigma_2), \quad (4.7)$$

where f_i, f_j are the Fermi distribution functions and i, j represent a set of indices (k, n, p, q). In our case there are two contributions to the interaction potential $G(\xi_1, \xi_2)$; one is the bare Coulomb repulsion and the other is the attraction potential mediated by the substrate, namely, image potential.[29] Thus $G(\xi_1, \xi_2)$ is given as

$$G(\xi_1,\xi_2) = \frac{1}{|\pi_1 - \pi_2|} - \frac{K-1}{K+1} \frac{1}{\sqrt{(\vec{x}_1 - \vec{x}_2)^2 + (z_1 + z_2)^2}}$$

$$= \int d^2Q \frac{1}{2\pi Q} e^{i\vec{Q}\cdot(\vec{X}_1-\vec{X}_2)} \left\{ e^{-Q|z_1-z_2|} - \frac{K-1}{K+1} e^{-Q(z_1+z_2)} \right\} . \quad (4.8)$$

In the above Q and X are 2- dimensional momentum and coordinates vectors parallel to the surface, respectively. Inserting eqs. (4.7), (4.8) into eq. (4.6) and after taking summation over the spin coordinates, we finally obtain the RPA equation

$$\rho_{ind}(\pi,\omega) = 2\sum_{i,j} \frac{f_i - f_j}{\epsilon_i - \epsilon_j + \omega + i\delta} \phi_i^*(\pi)\phi_j(\pi) \int d\pi_1 d\pi_2 \phi_i(\pi_1)\phi_j^*(\pi_1)$$
$$\times \int d^2Q \frac{1}{2\pi Q} e^{i\vec{Q}\cdot(\vec{X}_1-\vec{X}_2)} \left\{ e^{-Q|z_1-z_2|} - \frac{K-1}{K+1} e^{-Q(z_1+z_2)} \right\}$$
$$\times \left\{ \rho_{ind}(\pi_2,\omega) + \rho_{ext}(\pi_2,\omega) \right\} . \quad (4.9)$$

Next let us consider the solution of this equation for the parallel rod model. We put $\rho_{ext}(r,\omega)$ equal to $\exp(iQX)\,\rho_{ext}(Z)$ to discuss the charge fluctuation with a crystal wave vector Q. From eqs. (4.1), (4.9), we find $\rho_{ind}(r,\omega)$ can be expanded as

$$\rho_{ind}(\pi) = \sum_{\nu} D(\nu)\ \Phi(\vec{Q},\nu,\pi) \quad (4.10)$$

$$\Phi(\vec{Q},\nu,\pi) = \frac{1}{\sqrt{L}} e^{iQ_y y} \sum_n \frac{1}{\sqrt{N}} e^{iQ_x na}$$
$$\times \sin\left(\frac{p_1\pi}{\ell_1}(x-na)\right) \sin\left(\frac{p_2\pi}{\ell_1}(x-na)\right) \sin\left(\frac{q_1\pi}{\ell_2}z\right) \sin\left(\frac{q_2\pi}{\ell_2}z\right) , \quad (4.11)$$

where ν represents a set of indices (p_1, p_2, q_1, q_2). The correspondence of the pair band indices (p_1, p_2, q_1, q_2) and the mode index ν are listed in Table 4.1. Substituting the

expression (4.10) in two eq. (4.9), we obtain the following matrix equation for expansion coefficients D(ν)

$$\left\{ \delta_{\nu\nu'} - \chi(Q_y,\omega,\nu) I(\vec{Q},\nu,\nu') \right\} D(\nu') = \chi(Q_y,\omega,\nu) J(\vec{Q},\nu). \quad (4.12)$$

In the above, $\chi(Q,\omega,\nu)$ is the polarization function defined by

$$\chi(Q,\omega,\nu) = \frac{2\pi}{L} \sum_k \frac{f_{k-Q}^{P_2\beta_2} - f_k^{P_1\beta_1}}{\epsilon_{k-Q}^{P_2\beta_2} - \epsilon_k^{P_1\beta_1} + \omega + i\delta}$$
$$+ (1 - \delta_{P_1P_2}\delta_{\beta_1\beta_2}) \frac{2\pi}{L} \sum_k \frac{f_{k-Q}^{P_1\beta_1} - f_k^{P_2\beta_2}}{\epsilon_{k-Q}^{P_1\beta_1} - \epsilon_k^{P_2\beta_2} + \omega + i\delta}. \quad (4.13)$$

$I(Q,\nu,\nu')$ and $J(Q,\nu)$ are the matrix elements between $\Phi(Q,\nu,r)$ and $\Phi(Q,\nu',r)$, and between $\Phi(Q,\nu,r)$ and $\exp(iQX)\ \rho_{ext}(Z)$, respectively. They are written as follows;

$$I(\vec{Q},\nu,\nu') = \frac{16}{\pi \ell_1^2 \ell_2^2} \int d\pi_1 d\pi_2 \Phi^*(\vec{Q},\nu,\pi_1) G(\pi_1,\pi_2) \Phi(\vec{Q},\nu',\pi_2)$$
$$= \sum_{\vec{G}} \frac{2}{a|\vec{Q}+\vec{G}|} \left\{ \frac{2}{\ell_1} \int_0^{\ell_1} dx \sin\left(\frac{P_1}{\ell_1}\pi x\right) \sin\left(\frac{P_2}{\ell_1}\pi x\right) e^{i(Q_x+G_x)x} \right\}$$
$$\times \left\{ \frac{2}{\ell_1} \int_0^{\ell_1} dx \sin\left(\frac{P_1'}{\ell_1}\pi x\right) \sin\left(\frac{P_2'}{\ell_1}\pi x\right) e^{-i(Q_x+G_x)x} \right\}$$
$$\times \left\{ \left(\frac{2}{\ell_2}\right)^2 \int_0^{\ell_2} dz_1 dz_2 \sin\left(\frac{\beta_1}{\ell_2}\pi z_1\right) \sin\left(\frac{\beta_2}{\ell_2}\pi z_1\right) \right.$$
$$\left. \times \left(e^{-|\vec{Q}+\vec{G}||z_1-z_2|} - \frac{K-1}{K+1} e^{-|\vec{Q}+\vec{G}|(z_1+z_2)} \right) \sin\left(\frac{\beta_1'}{\ell_2}\pi z_2\right) \sin\left(\frac{\beta_2'}{\ell_2}\pi z_2\right) \right. \quad (4.14)$$

$$J(\vec{Q},\nu)=\frac{16}{\pi l_1^2 l_2^2}\int d\pi_1 d\pi_2\ \Phi^*(\vec{Q},\nu,\pi)\,G(\pi_1,\pi_2)\,e^{i\vec{Q}\cdot\vec{X}_2}\rho_{ext}(z_2)$$

$$=\frac{4}{l_1|\vec{Q}|}\left(\frac{2}{l_1}\int_0^{l_1}dx\,\sin\left(\frac{p_1}{l_1}\pi x\right)\sin\left(\frac{p_2}{l_1}\pi x\right)e^{iQ_x x}\right)$$

$$\times\left(\frac{2}{l_2}\right)^2\int_0^{l_2}dz_1 dz_2\,\sin\left(\frac{q_1}{l_2}\pi z_1\right)\sin\left(\frac{q_2}{l_2}\pi z_1\right)$$

$$\times\left(e^{-Q|z_1-z_2|}-\frac{K-1}{K+1}e^{-Q(z_1+z_2)}\right)\rho_{ext}(z_2),\qquad (4.15)$$

where $G=(2\pi n/a,0,0)$ $(n=0,\pm1,\pm2,\cdots)$ is the reciprocal lattice vector.

If the frequency of the external field is equal to the plasmon frequency, finite charge fluctuation is induced by an infinitesimal external field. Thus the plasmon energy is determined by the condition that eq. (4.12) for no eternal field (J=0) has a nontrivial solution, namely,

$$\det\left\{\delta_{\nu\nu'}-\chi(Q_y,\omega,\nu)I(\vec{Q},\nu,\nu')\right\}=0\qquad .\ (4.16)$$

C. Plasmon Dispersion in small Q Regions

In the following, we consider the lowest three modes $(p,q)=(1,1),(1,2),(2,1)$ that can be regarded as K-4s, $4p_z$, $4p_x$ orbitals, respectively. We assume the higher bands ε_k^{12} and ε_k^{21} to be empty, while assuming the lowest one ε_k^{11} to be occupied if the absolute value of k is less than Fermi wave number k_f. As shown in Fig. 4. 3, there exist three kinds of coupled excitation modes; the 4s-4s intraband mode ($\nu=1$), the 4s-$4p_z$ interband mode ($\nu=2$), the 4s-$4p_x$ interband

mode (ν=3), and the matrix in the left hand side of eq. (4.16) becomes 3×3. As nondiagonal matrix elements $I(Q, \nu, \nu')$ are rather smaller than the diagonal one in small Q regions, we at first use the approximation to treat the three modes independently. Such a procedure is quite helpful to emboss the physical picture of each excitation mode. In this approximation, eq. (4.12) reduces to

$$\chi(Q_y, \omega, \nu)\, I(\vec{Q}, \nu, \nu) = 1 \quad (\nu = 1, 2, 3) \quad . \tag{4.17}$$

Now let us clarify charasteristic features of each plasmon mode by solving eq. (4.17).

(1) ν=1 4s-4s intraband mode

If Q is small, $\chi(Q, \omega, 1)$ is approximated as

$$\chi(Q_y, \omega, 1) = \frac{2k_f}{m\omega^2} Q_y^2 = \frac{2k_f}{m\omega^2} Q^2 \cos^2\theta \quad , \tag{4.18}$$

where θ is the angle between $\vec{Q}$ and rod axis. Keeping only G=0 term in eq. (4.14), $I(Q, 1, 1)$ is expanded as

$$I(\vec{Q}, 1, 1) \cong \frac{2}{aQ}\left\{ \frac{2}{\kappa+1} + \left(\frac{5}{4\pi^2} - \frac{1}{3} + \frac{\kappa-1}{\kappa+1}\right) l_2 Q + \cdots \right\}. \tag{4.19}$$

From eqs. (4.17)-(4.19), we obtain the plasmon dispersion

$$\omega^2(\vec{Q}) = \frac{2k_f}{ma}\left\{ \frac{2}{\kappa+1} + \left(\frac{5}{4\pi^2} - \frac{1}{3} + \frac{\kappa-1}{\kappa+1}\right) l_2 Q \right\} Q \cos^2\theta. \tag{4.20}$$

As the Fermi wave number k_f is related to the average electron density of the overlayer by $k_f = \pi a l_2 n/2$, eq. (4.20)

can be rewritten as

$$\omega(\vec{Q}) = \omega_p \left(\frac{l_2 Q}{2}\right)^{1/2} \left\{ \frac{2}{\kappa+1} + \left(\frac{5}{4\pi^2} - \frac{1}{3} + \frac{\kappa-1}{\kappa+1}\right) l_2 Q \right\}^{1/2} \cos\theta , \quad (4.21)$$

where ω_p is the plasma frequency of the overlayer, namely, $4\pi n/m$. This mode is essentially the same as the A-mode of Newns' model.

If the dielectric constant of the substrate is unity, the dispersion is proportional to $Q^{1/2}$ and it becomes identical as the plasmon dispersion of the uniform thin film derived by Stern[30] classically except for the factor $\cos\theta$. On the other hand, if the substrate is a perfect conductor ($\kappa=\infty$), the interaction between electrons becomes a short range one due to the image charge in the substrate and the dispersion is proportional to Q with a character of acoustic wave. The meaning of factor $\cos\theta$ is clear. This mode is essentially caused by the charge fluctuation in the direction parallel to rectangular rods. Therefore it can oscillate most strongly along the chain ($\theta=0°$) and can not oscillate perpendicularly to the chain ($\theta=90°$). Due to the condition

$$\int d\pi \, \rho_{ind}(\pi, \omega) = 0 , \quad (4.22)$$

the intraband mode is not able to have any charge fluctuation at Q=0 irrespective of the form of the interaction potential as can be seen by setting $\nu=1$ and Q=0 in eq. (4.11). This means the dispersion of the 2-dimensional intraband plasmon must converge to $\omega=0$ in the limit of Q=0 in any case.

(2) $\nu=2$ $4s-4p_z$ interband mode

If Q is small, $\chi(Q,\omega,2)$ is approximated as

$$\chi(Q_y,\omega,2)=\frac{4\omega_{12}k_f}{\omega^2-\omega_{12}^2} \quad , \quad (4.23)$$

where $\omega_{12}=3\pi^2/(2\mu_2 l_2^2)$ is the energy difference between 4s-band and $4p_z$-band. As is done in deriving eq. (4.19), keeping only G=0 term in eq. (4.14), we obtain

$$I(\vec{q},2,2)\cong\frac{2}{aQ}\left\{\frac{10l_2}{9\pi^2}Q-\left(\frac{16l_2}{9\pi^2}\right)^2Q^2-\frac{K-1}{K+1}\left(\frac{16l_2}{9\pi^2}\right)^2Q^2+\cdots\right\}. \quad (4.24)$$

From eqs. (4.17), (4.23), (4.24) the dispersion of the $4S-4P_z$ interband plasmon is written as

$$\omega^2(\vec{q})=\omega_{12}^2+\frac{8\omega_{12}}{a}k_f\left\{\frac{10l_2}{9\pi^2}-\frac{2K}{K+1}\left(\frac{16l_2}{9\pi^2}\right)^2Q\right\} \quad . \quad (4.25)$$

The plasmon energy is larger than the single particle excitation energy ω_{12} by the second term of eq. (4.25). This shift is called as depolarization shift. To interpret it, it is convenient to suppose electrons to be classical point charges bound with frequency ω_{12}. When the electrons oscillate collectively they feel not only the force which bound them but also electric field induced by the charge fluctuation. Therefore the eigenfrequency of the collective mode is increased and exceeds ω_{12}. The $4s-4p_z$ mode is an oscillation perpendicular to the surface and essentially the same as the B-mode in Newns' model. The dispersion is linearly with negative gradient and moreover it is

isotropical in small Q regions though the electronic structure is extremely anisotropic.

Recently Nakayama et al discussed the general properties of inter-surface-band plasmon in small Q regions with the RPA[31] and also came to the conclusion that plasmon mode which has a polarization field perpendicular to the surface has negative linear dispersion at Q=0. However, they did not clarify its origin. So let us make clear the physical meaning of the negative linear dispersion taking our model as an example. From eq. (4.25) we see the negative linear dispersion means the decrease of the depolarization shift with increasing Q. Actually as shown in Fig. 4.4a, all the rods oscillate in phase at Q=0 and the polarization field of a rod is reinforced by those of neighboring rods. This results in the largest depolarization shift for Q=0. On the other hand the adjacent rods begin to oscillate in antiphase as Q deviates from zero and the polarization field of a rod is partially canceled by those of neighboring ones. (see Fig. 4.4b) Thus the depolarization shift becomes smaller and the negative linear dispersion is realized.

(3) $\nu=3$ $4s-4p_x$ interband mode

$\chi(Q,\omega,3)$ has the same form with $\chi(Q,\omega,2)$ in eq. (4.23) with ω_{12} set equal to $3\pi^2/(2\mu_1 l_1^2)$. To estimate $I(Q,3,3)$ we retain all the terms with $G\neq 0$ together with $G=0$ term for the present case. Then it is expanded as

$$I(\vec{q},3.3) \cong \frac{2}{a} q \sin^2\theta \frac{2}{K+1}\left(\frac{16 l_1}{9\pi^2}\right)^2 + \left(\alpha - \frac{K-1}{K+1}\beta\right) + \cdots \quad (4.26)$$

where α and β ($\alpha>\beta>0$) are the contributions from terms with $G\neq 0$ evaluated at $Q=0$. They are defined by

$$\alpha-\frac{K-1}{K+1}\beta=\sum_{G\,(\neq 0)}\left|\frac{2}{\ell_1}\int_0^{\ell_1}\sin\left(\frac{\pi}{\ell_1}x\right)\sin\left(\frac{2\pi}{\ell_1}x\right)e^{iG_x x}dx\right|^2$$

$$\times\left\{\left(\frac{2}{\ell_2}\right)^2\int_0^{\ell_2}dz_1dz_2\,\sin^2\left(\frac{\pi}{\ell_2}z_1\right)\left(e^{-G|z_1-z_2|}-\frac{K-1}{K+1}e^{-G(z_1+z_2)}\right)\sin^2\left(\frac{\pi}{\ell_2}z_2\right)\right\}. \quad (4.27)$$

From eqs. (4.17), (4.23), (4.26) we obtain the dispersion of the $4s-4p_x$ interband plasmon

$$\omega^2(\vec{Q})=\omega_{12}^2+4\omega_{12}k_f\left(\alpha-\frac{K-1}{K+1}\beta\right)+\frac{16\omega_{12}k_f}{\alpha(K+1)}\left(\frac{16\ell_1}{9\pi^2}\right)^2 Q\sin^2\theta. \quad (4.28)$$

This mode is characteristic of the anisotropic chain structure of the present model and does not exist in uniform thin film models advanced so far. The dispersion depends on Q positive linearly. The slope of the dispersion at Q=0 is proportional to $\sin^2\theta$ and thus becomes the largest at $\theta=90°$. The polarization field of this mode is vertical both to the rod axes and to the surface normal. Nakayama et al[31] also showed the inter-surface-band plasmon which polarizes parallel to the surface has a positive linear dispersion at Q=0. According to their theory, however, such a mode can not have a depolarization shift at Q=0. But as revealed later, this is not necessarily the case and the contribution of the second term in eq. (4.28) is quite important. Now let us clarify the physical meaning of the positive linear dispersion of this mode at Q=0. In contrast to the case of

the $4s-4p_z$ mode, this implies the increase of the depolarization shift as Q increases. In fact the polarization field of a rod is damaged most by those of neighboring rods when they oscillate in phase, that is, at Q=0 as illustrated in Fig. 4. 5a. Thus the depolarization shift becomes the smallest at Q=0. On the other hand cancellation of the polarization field of a rod by those of the others becomes smaller as Q deviates from zero and correspondingly the depolarization shift increases by degrees. (see Fig. 4. 5b) This is the origin of the positive linear dispersion in small Q regions.

D. Plasmon Dispersion in the General Q Region

We solved eq. (4. 16) exactly in general Q regions and obtained dispersions of three coupled plasmon modes. The plasmon dispersions for $\theta=45°$ is shown in Fig. 4. 6. Here the side lengths of a rod l_1, l_2 are chosen to be 7(a. u.) which is nearly the diameter of K atom. The interval between neighboring rods a is determined by the geometry of the surface and is set equal to 14. 2(a. u.). We choose Fermi wave number k_f as $\pi/(2l_1)$ for each rod to contain one electron per length l_1. The interband transition energy $\omega_{12}=3\pi^2/(2\mu_1 l_1^2)=3\pi^2/(2\mu_2 l_2^2)$ are adjusted as 0. 59(eV) in order that interband plasmon energies roughly reproduce the observed plasmon peak. The dielectric constant of the substrate $\varkappa$ is set equal to 15.

Near Q=0, the plasmon modes $\omega_1, \omega_2, \omega_3$ in fig. (4. 6) correspond to the $4s-4s(\nu=1)$, $4s-4p_z(\nu=2)$, $4s-4p_x(\nu=3)$ mode, respectively and each dispersion has the features

explained above. Especially, the $4s-4p_x$ ($\nu=3$) mode is found to have a large depolarization shift at Q=0 owing to the second term of eq. (4.28). Nakayama et al failed to predict such behaviour of this mode. In large Q regions, the characters of ω_1 and ω_2 modes interchange with each other smoothly on account of the nondiagonal matrix elements of eq. (4.16). The shaded regions indicate the single particle excitation energies. The calculated plasmon energies increase in large Q regions reflecting the increase of the maximum of the single particle excitation spectrums while the observed plasmon energy is saturated in large Q regions. This disagreement will be easily resolved if we take account of the finite band width along the chain direction.

E. Summary and Discussions

Starting from the simplified parallel rod model, we obtained three coupled plasmon modes. Especially the $4s-4p_x$ ($\nu=3$) mode which is characteristic of the anisotropic chain structure is able to reproduce the three important features of the observed plasmon dispersion[1], namely, the finite energy at Q=0, the positive linear dispersion and the azimuth dependent anisotropy of the dispersion. So this mode is expected to be responsible for the main loss peak of the AREELS observation. The slope of its dispersion at Q=0 becomes the largest when $\theta=90°$. Thus the observed plasmon dispersion in the left hand side of Fig. 3.4 may well be assigned to that of the (1,−1,0) azimuth. The reason why the dispersion of the (1,1,0) azimuth is not detected is simply understood by the following arguments. Suppose an electron

to be incident on the surface. When it excites a $4s-4p_x$ plasmon with 2-dimensional wavevector $Q=(q_x, q_y, 0)$, it looses the momentum $Q'=(q_x, q_y, q_z)$ because of the conservation of the momentum components parallel to the surface. Here q_z is determined from the condition of the energy conservation. This momentum change of the incident electron induces an external field proportional to $\exp(iQ'\hat{x})$ in the system and by this field the plasmon is excited. However, before the excitation becomes collective, single particle excitations from 4s-band to $4p_x$-band must be generated by the external field. The probability is in proportion to

$$\left| \int \varphi_{4s}(\pi)\, \varphi_{4P_x}(\pi)\, e^{i\vec{Q}'\cdot\vec{\pi}}\, d\pi \right|^2 \qquad (4.29)$$

This become the largest for the (1,-1,0) azimuth and is completely zero for the (1,1,0) azimuth due to the symmetry of the 4s and $4p_x$ orbitals. Therefore only the plasmon dispersion of the (1,-1,0) azimuth can be detected by AREELS observations.

5. Electronic Structure of Si(100)2×1-K Surface

In the last section we showed that the observed plasmon dispersion can be explained fairly well provided that there are two surface bands near the Fermi level; one is the 4s-like band which is partially filled, and the other is the $4p_x$-like band which is empty. In the real system the band structure of the alkali overlayer might change drastically from such a simplified model due to the charge transfer from K atoms to the substrate Si. To elucidate the electronic structure of the Si(100) 2×1-K surface at the full coverage qualitatively as well as quantitatively, we perform the self-consistent band calculation in this section.

A. Model

We adopt two kinds of structure models as candidates for the Si(100) 2×1-K surface. The first one, that is called Model-1 in the following, is the original Levine's model.[24] In this model, the Si atoms in the top layer are assumed to form symmetric dimers and the K atoms sit on the four-fold hollow site between two dimers. The second one that is called Model-2 is for the most part identical as Model-1, but the K atoms are assumed to sit on the bridge site of a dimer instead of the hollow site. The reason why we take two structure models is as follows. Though it is almost established that alkali atoms are located on the ridge of the Si dimers to make one-dimensional chains, the precise adsorption site of the K atom appears still remaining unknown. Thus it is quite interesting to examine the change

of the electronic structures by slightly modifying the construction of the surface and to extract the common features about the electronic structure in such a peculiar "chain" system.

The surface band structures are calculated using the thin film models KSi_8H_4. Fig. 5.1a shows the side view of the thin film Model-1, which is the same as that of Model-2. Figs. 5.1b and 5.1c show the top view of Model-1 and 2, respectively. The thin film consists of the K overlayer, four Si layers which include the dimer atoms and the H overlayer on the backside surface. The hydrogen atoms are adsorbed to eliminate the dangling bonds of the backside surface. The unit cell of the thin film contains one K atom, eight Si atoms and four H atoms. We assigned a number (1~8) to each Si atom in the unit cell. The configuration of the substrate Si is assumed identical as that of the bulk Si except for the top dimer layer. The bond length between neighboring Si atoms is 2.3(Å) and we use the same value for the Si-Si bond length of a dimer. The distance between the K atom and the closest Si atom of a dimer is chosen to be equal to the sum of K and Si atomic radii, 3.52(Å). The Si-H distance is determined in the same way and set equal to 1.68(Å). The point group at a K site is C_{2v}; there are two mirror planes and C_2 axis.

Since the asymmetric dimer is presumed superior to the symmetric one with respect to the bare Si(100) 2×1 surface, it must be intriguing to calculate the electronic structure of the Si(100) 2×1-K surface with the asymmetric dimers. However, we have not performed it yet. One of the reasons is that it takes more computational time on account of its

lower symmetry. But it should be remarked that the mechanism which stabilizes the asymmetric dimer as compared to the symmetric one would not work for the alkali covered surface because of the significant charge transfer between the alkali atom and dimer.

B. Method of the Band Calculation

The present band calculation is carried out by the numerical LCAO-Xα-SCF method.[32] We summarize the essence of the calculational method briefly below.

The Bloch functions is written as

$$\mathcal{G}_{\alpha\lambda}(k,r) = \frac{1}{\sqrt{N}} \sum_{l} e^{ik(l+r_\alpha)} \phi_{\alpha\lambda}(r-l-r_\alpha), \quad (5.1)$$

where k is a crystal momentum, l is a lattice vector, r_α is the coordinates vector of the α-th atom in the unit cell and $\phi_{\alpha\lambda}$ is the λ-th atomic orbital of the α-th atom. $\phi_{\alpha\lambda}$ is calculated numerically with the spherically averaged crystal potential around each atom. We use eighty atomic orbitals, that is, H-1s, Si-2s,2p,3s,3p, K-2s,2p,3s,3p,4s,4p orbitals as basis atomic orbitals and Si-1s and K-1s orbitals are regarded as core states. We expand the n-th band wavefunction as

$$\psi_{nk}(r) = \sum_{\alpha\lambda} C_{\alpha\lambda}(n,k)\, \mathcal{G}_{\alpha\lambda}(k,r) \quad . \quad (5.2)$$

By the variational principle the secular equation for coefficients $C_{\alpha\lambda}(n,k)$ is written as

$$\sum_{\alpha_2\lambda_2} \langle \varphi_{\alpha_1\lambda_1} | \mathcal{H} | \varphi_{\alpha_2\lambda_2} \rangle C_{\alpha_2\lambda_2}(n.k)$$

$$= \epsilon(n.k) \sum_{\alpha_2\lambda_2} \langle \varphi_{\alpha_1\lambda_1} | \varphi_{\alpha_2\lambda_2} \rangle C_{\alpha_2\lambda_2}(n.k) \quad , \text{(5.3)}$$

where

$$\mathcal{H} = T_{kin} + V_{Coul} + V_{ex} \qquad \text{(5.4)}$$

is the one electron Hamiltonian made of three parts. The first term T_{kin} is the kinetic energy of an electron. V_{coul} is the Coulomb potential given by

$$V_{Coul}(r) = \int \frac{\rho(r')}{|r-r'|} dr' - \sum_{l\alpha} \frac{Z_\alpha}{|r-l-r_\alpha|} \quad , \text{(5.5)}$$

where $\rho(r)$ is the electron density and Z_α is the atomic number of the α-th atom. V_{ex} represents the exchange-correlation potential and is expressed in $X\alpha$ approximation as

$$V_{ex}(r) = -3\alpha \left(\frac{3}{\pi}\rho(r)\right)^{1/3} \qquad (\alpha = 0.7) \quad . \text{(5.6)}$$

The matrix elements and the overlap integrals in eq. (5.4) are numerically evaluated by the 3-dimensional Diophantine method.[33] We take about 9600 integration sampling points in a unit cell.

Once the secular equation (5.3) is solved, the electron density is obtained as follows;

$$\rho(r) = \sum_{l\alpha} \left\{ \rho_\alpha^{Core}(r-l-r_\alpha) + \rho_\alpha^{v}(r-l-r_\alpha) \right\} \qquad \text{(5.7)}$$

$$\rho_\alpha^v(r) \cong \frac{1}{N}\sum_{\substack{\lambda \\ \alpha_1\lambda_1}}\left\{\sum_{\substack{n.k \\ \epsilon(n.k)\le\epsilon_f}} C^*_{\alpha_1\lambda_1}(n.k)\langle\varphi_{\alpha_1\lambda_1}|\varphi_{\alpha\lambda}\rangle C_{\alpha\lambda}(n.k)\right\} \times \varphi^2_{\alpha\lambda}(r) \quad . (5.8)$$

Here $\rho_\alpha^{core}(r)$ and $\rho_\alpha^{v}(r)$ are the core and the valence electron charge of the α-th atom. For $\rho_\alpha^{v}(r)$ the Mulliken's population analysys is used. The k-space integral in eq. (5.8) is carried out by the tetrahedron method of Lehmann et al.[34]

To perform the self-consistent calculation, we first input some arbitrary atomic charges. Following the method explained in the above, we obtain the output atomic charges and then these are in turn used as the input atomic charges. Such iterative procedures are repeated until the self-consistency of the electron density is achieved. About ten iterations are required for the convergence of the $\rho(r)$ in the present calculation.

C. Results of the Band Calculation

To test the validity of our band calculation, we first calculated the band structure of the bare Si(100) 2×1 surface with the thin film model Si_8H_4 which is obtained from KSi_8H_4 by removing K atom. The resultant band structure near the Fermi level ε_f is shown in Fig. 5.2 together with BZ and the notation of symmetry points. The bands with bulklike characters are located in shaded regions. There appear two surface bands in the gap region. The lower band

has the character of the bonding π orbital while the upper one has the character of the antibonding π^* orbital composed of two dangling bonds of a dimer. The obtained band structure is almost the same as that proposed by Ihm, Cohen and Chadi[35] using the pseudepotential method. Thus the present slab model KSi_8H_4 is also supposed to work well to reveal the band structure of the Si(100) 2×1-K surface.

The calculated band structures of KSi_8H_4 for Model-1 and Model-2 are shown in Figs. 5.3 and 5.4, respectively, in the energy region near ε_f. The Fermi level ε_f crosses the 59-th energy band which is counted from the lowest one. For Model-1 the 58-th band also has a small Fermi surface. Three electrons per unit cell are accomodated in the 58-th and the 59-th bands. The 58-th, 59-th and 60-th bands are called hereafter as A, B and C bands, respectively. These three bands are surface bands composed mainly of K valence states and those of a dimer as discussed below. Other bands with bulklike characters are situated in the shaded regions. It should be noted that our band calculations do not reproduce the correct band gap of the substrate Si because they are obtained with thin film models which include only four Si layers. But this is not crucial at all as we are mainly interested in the surface band structures, which would be reproduced with the thin film model so long as the charge tranfer between the overlayer and the substrate is adequately described by it. Fig. 5.6 shows the total density of states of the KSi_8H_4 thin film for Model-1. The three sharp peaks near ε_f correspond to the surface bands A, B, C, respectively.

By comparing Fig. 5.3 with Fig. 5.4, we find overall band

dispersions of surface bands are common to Model-1 and Model-2 except for some detailed points such as width of each band and relative energy differences between them. Owing to the chain structure of the Si(100) 2×1-K surface, the energy dispersion of each surface band is generally smaller along the G-X and Y-S axes than along the G-Y and X-S axes. But the band B has a rather large energy change along the G-X axis as compared with the other bands. This can be ascribed to the interaction between the chains mediated by the substrate Si, particularly by the 6-th Si atom in unit cell.

Next, orbital characters of the three surface bands will be discussed minutely because they are closely related with the dispersion of the overlayer plamon. Since the orbital components of each band do not change along the direction perpendicular to the chain, it is convenient to dicuss them separately in three regions of BZ, that is, near the G-X axis, near the Y-S axis and between the former two regions.

(1) near the G-X axis

The origin of the bands A,B,C near the G-X axis in BZ is common to Model-1 and Model-2 and can be understood schematically as illustrated in Fig. 5.6. The wavefunction of the surface band A is mainly made of the antibonding combination of the K-4s and the bonding σ orbital of a dimer. It also contains the π orbital of a dimer with a little smaller weight. The wavefunction of the band B is mostly contributed from the bonding combination of $4p_x$ orbital of K and 3s, π^* orbital of a dimer. On the other hand, the wavefunction of the band C is mainly made of the

bonding combination of K-4p_z orbital and the π orbital of a dimer with a considerable admixture of K-4s orbital. The interaction between K-4s,4p_x states and the π^*, σ states of a dimer is effectively larger in Model-1 than in Model-2 since K atom has two adjacent dimers in Model-1 while it has only one in Model-2. Thus Model-1 exceeds model-2 both in the energy lowering of the band B and in the energy rising of the band A. Therefore the energy gap between the bands A,B of Model-1 (~0.7(eV)) becomes smaller than that of Model-2 (~1.1(eV)). In contrast to this, the interaction between K-4p_z state and the π state of a dimer becomes larger in Model-2 than in Model-1 owing to the large overlap of the two orbitals. This results in the larger energy lowering of the band C near the G-X axis for Model-2.

(2) near the Y-S axis

The orbital components of valence states of the substrate Si are for the most part the same as those near the G-X axis for both Model-1 and Model-2. The band B also contains 3p_y orbital of the 3-rd and the 4-th Si atoms near this axis. On the other hand, weights of K valence states in the bands A,B,C are considerably reduced and each surface band comes to have the character of the dangling bond band of a dimer. Especially for Model-1, orbital components of K valence states change rather drastically. Due to the symmetry determined by the orbital components of the substrate Si (mainly of a dimer), K orbital states can not be contained along the Y-S axis in the band B and the only K-4p_y is allowed to be included in the bands A,C. Hence, the bands A,C have small amount of K-4p_y in place of K-4s,4p_z.

(3) between the G-X axis and the Y-S axis

As the wave vector changes along the G-Y and the X-S axis, the orbital components of the three bands vary continuously from those near the G-X axis to those near the Y-S axis. But there appear substantial admixture of K-4p_y around the middle of the G-Y and the X-S axis for the band C of Model-2. The large energy increase of the band C along the G-Y and the X-S axis is due to the K-4s component in it while the large energy decrease of the band B reflects 3-p_y of the 3-rd and the 4-th Si atoms.

For Model-1 we also calculated the surface band structure setting the K-Si distance equal to 3.0(Å) instead of 3.5(Å). This makes the interaction between K chains and the substrate larger and thus the energy gap between the bands A,B near the G-X axis becomes still smaller (~0.54(eV)). But the overall surface band structure remained almost unchanged.

Finally we mention about the charge distribution of the surface. According to the Mulliken's population analysis, the charge transfer from K atom to the substrate is about 0.13 electron for Model-1 and about 0.09 elctron for Model-2. These values are rather small as compared with those in low coverages where it is known alkali atoms completely become ions. The Si atom of a dimer becomes negative about -0.08 electron in Model-1 and about -0.09 electron in Model-2.

D . Summary and Discussions

We have calculated the band structure of the Si(100) 2×1-K surface self-consistently with two kinds of structure models which have different K adsorption sites. Roughly speaking, the surface band structure of Model-1 is the same as that of Model-2; the surface becomes metallic at the full coverage and three surface bands A,B,C appear near the Fermi level ε_f. We also find that the overall band structure does not change against the slight shift of K atom along the surface normal so much. Thus we are convinced that the surface band structure obtained in this section does not suffer serious modifications against slight structure changes.

The surface bands A,B,C have the character of K-4s, $4p_x$, $4p_z$ orbitals near the G-X axis, respectively. Near the G-X axis, the band A is occupied while the band B is empty. Therefore the inter-surface-band plasmon between the bands A,B is conceived as a best candidate of the observed plasmon loss peak.

6. Dispersion of the Overlayer Plasmon based on the the Surface Band Calculation

A. Theoretical Formulation

(1) Matrix Equation

In this section we calculate the dispersion of the overlayer plasmon by a non-empirical way based on the surface bands calculated in section 5. For this purpose we are required to solve the RPA equation derived in section 4,

$$\rho_{ind}(\pi,\omega) = 2\sum_{\substack{n_1 n_2 \\ k_1 k_2}} \frac{f_{n_1k_1} - f_{n_2k_2}}{\epsilon(n_1k_1) - \epsilon(n_2k_2) + \omega + i\delta} \phi^*_{n_1k_1}(\pi)\phi_{n_2k_2}(\pi)$$

$$\times \int d\pi_1 d\pi_2 \phi_{n_1k_1}(\pi_1)\phi^*_{n_2k_2}(\pi_1)\frac{1}{|\pi_1 - \pi_2|}\left\{\rho_{ind}(\pi_2,\omega) + \rho_{ext}(\pi_2,\omega)\right\}, \quad (6.1)$$

where $\varepsilon(n,k)$ and $\phi_{nk}(r)$ are the energy and the wavefunction of the electron obtained from the band calculation in section 5, respectively. The index k denotes the 2-dimensional wavevector and n is the band index. In the above, all the bulklike states are understood to be included in summation over n_1, n_2 thus the image potential in eq. (4.9) which originates from the interaction between electrons in surface states and those in bulk states are omitted in the present case.

To solve the integral equation (6.1), it is convenient to cast it in a matrix form using some basis set. The use of the Wannier function is quite useful for this purpose. The wavefunction $\phi_{nk}(r)$ is written in terms of the Wannier function of the n-th band as

$$\phi_{nk}(r) = \frac{1}{\sqrt{N}} \sum_{\ell} e^{ik\cdot\ell} W_n(r-\ell) \quad , \quad (6.2)$$

where the Wannier function $W_n(r)$ is defined by

$$W_n(r) = \frac{1}{\sqrt{N}} \sum_{k} \phi_{nk}(r) \quad . \quad (6.3)$$

In the above, $W_n(r)$ is not determined uniquely due to the uncertainty of the phase factor of $\phi_{nk}(r)$. By choosing it suitably we make the Wannier function $W_n(r)$ be a real function and localized at r=0 as well as possible. To consider the charge fluctuation with a crystal momentum Q, $\rho_{ext}(r)$ is put equal to $\exp(iQX)\,\rho_{ext}(Z)$ in the following. Then only the terms with $k_1 = k_2 - Q$ are left in eq. (6.1) and the product of two wavefunctions in eq. (6.1) is written as

$$\phi^{*}_{m,k-Q}(r)\,\phi_{n,k}(r) = \left\{\frac{1}{\sqrt{N}} \sum_{\ell} e^{-i(k-Q)\ell} W_m(r-\ell)\right\}\left\{\frac{1}{\sqrt{N}} \sum_{\ell'} e^{ik\ell'} W_n(r-\ell')\right\}$$

$$= \sum_{d\,(=\ell'-\ell)} \frac{1}{\sqrt{N}} e^{ikd} \left\{\frac{1}{\sqrt{N}} \sum_{\ell} e^{iQ\cdot\ell} W_m(r-\ell) W_n(r-\ell-d)\right\} . \quad (6.4)$$

From eq. (6.4) we find the induced charge can be expanded as

$$\rho_{ind}(r,\omega) = \sum_{m\,n\,d} D(m,n,d)\,\Phi(\vec{Q},m\,n\,d,r) \quad (6.5)$$

$$\Phi(\vec{Q},m\,n\,d,r) = \frac{1}{\sqrt{N}} \sum_{\ell} e^{iQ\cdot\ell} W_m(r-\ell) W_n(r-\ell-d) \quad (6.6)$$

Here only the terms with $n \geqq m$ appear in eq. (6.5) as $\Phi(Q,n,m,d,r)$ is equal to $\Phi(Q,m,n,-d,r)$ and for the terms with m=n, either $\Phi(Q,m,m,d,r)$ or $\Phi(Q,m,m,-d)$ is included

in eq. (6.5). If the Wannier functions are well localized, contribution of terms with large |d| can be neglected.

Substituting the expression (6.5) in eq. (6.1), we obtain the following matrix equation for the expansion coefficients D(m, n, d)

$$\left\{ \delta_{\substack{m_1 n_1 d_1 \\ m_2 n_2 d_2}} - \chi(\vec{q}, \omega, m_1 n_1 d_1, d_3) I(\vec{q}, m_1 n_1 d_3 : m_2 n_2 d_2) \right\}$$

$$\times D(m_2 n_2 d_2) = \chi(\vec{q}, \omega, m_1 n_1 d_1, d_3) J(\vec{q}, m_1 n_1 d_3), \quad (6.7)$$

where repeated indices are understood to imply appropriate summation. In the above $\chi(Q, \omega, m, n, d, d')$ is the polarization function defined by

$$\chi(\vec{q}, \omega, m\, n\, d, d')$$

$$= \frac{2}{N} \sum_k \frac{f_{m\cdot k-q} - f_{n\cdot k}}{\epsilon(m\cdot k-q) - \epsilon(n\cdot k) + \omega + i\delta} e^{ik(d-d')}$$

$$+ \frac{2}{N} \sum_k \frac{f_{n\cdot k} - f_{m\cdot k+q}}{\epsilon(n\cdot k) - \epsilon(m, k+q) + \omega + i\delta} e^{-ik(d-d')} \qquad (n > m)$$

$$= \frac{2}{N} \sum_k \frac{f_{m\cdot k-q} - f_{m\cdot k}}{\epsilon(m\cdot k-q) - \epsilon(m\cdot k) + \omega + i\delta}$$

$$\times (e^{ikd} + e^{i(q-k)d} - \delta_{d0})(e^{-ikd'} + e^{-i(q-k)d'} - \delta_{d'0}) \qquad (n = m)$$

. (6.8)

I(Q, m, n, d, m', n', d') and J(Q, m, n, d) are the matrix elements of Coulomb potential between Φ(m, n, d, r) and Φ(m', n', d', r), and between Φ(m, n, d, r) and exp(iQX) ρ(Z), respectively. They are written as follows;

$$I(\vec{q}, mnd : m'n'd')$$

$$= \int d\pi_1 d\pi_2 \, \Phi^*(\vec{q}, mnd, \pi_1) \frac{1}{|\pi_1 - \pi_2|} \Phi(\vec{q}, m'n'd', \pi_2) \qquad (6.9)$$

$$J(\vec{q}, mnd)$$

$$= \int d\pi_1 d\pi_2 \, \Phi^*(\vec{q}, mnd, \pi_1) \frac{1}{|\pi_1 - \pi_2|} e^{i\vec{q}\cdot\vec{x}} \rho_{ext}(z) \quad . \qquad (6.10)$$

(2) Dispersion and Intensity of The Plasmon

In the same way as the case of the parallel rod model in section 4, the plasmon energy is determined by the condition that eq. (6.7) for no external field (J=0) has the non-trivial solution, namely,

$$\det \left\{ \delta_{\substack{m_1 n_1 d_1 \\ m_2 n_2 d_2}} - \chi(\vec{q}, \omega, m_1 n_1 d_1, d_3) I(\vec{q}, m_1 n_1 d_3 : m_2 n_2 d_2) \right\} = 0 \quad (6.11)$$

However, if the plasmon energy is merged in the continuous energy spectrum of other single particle excitation modes, the plasmon peak becomes broad owing to the coupling with them and the zero point of determinent (6.11) corresponding to the plasmon becomes undecided. One way to elude the problem is to introduce a damping factor γ for the plasmon energy. (Then one can search the zero point of eq. (6.11) replacing ω by $\omega + i\gamma$.) But more practical way is to calculate the energy loss spectrum of the incident electron beam directly. Then by tracing the energy loss intensity around the plasmon frequency, one can find the center and the width of the plasmon peak along with the single

particle excitation spectrum where the plasmon is merged. We will explain the method adopting "classical trajectory approximation"[36~37] in the following.

In the classical trajectory approximation, the incident electron is regarded as a classical unit charge following some fixed trajectory. The external perturbation field of this electron induces a charge fluctuation determined by eq. (6.7) in the system. Then one can calculate the energy loss of the incident electron by evaluating the work which is done for the electron by the induced field along the trajectory.

As shown in Fig. 6.1, we consider the reflection energy loss that corresponds to LEED or RHEED observation. The trajectory of the electron is then written as

$$\vec{r}_e(t) = \begin{cases} (\vec{v}_{\parallel} t \,,\, z_0 - v_z t) & t < 0 \\ (\vec{v}_{\parallel} t \,,\, z_0 + v_z t) & t > 0 \end{cases} \quad , \quad (6.12)$$

where $v_{\parallel}$, v_z are the components of the velocity parallel and normal to the surface, and z_0 is the z-coordinates of the reflection point outside the surface. The external potential is then given by

$$\phi_{ext}(r, t) = \frac{1}{|r - r_e(t)|}$$
$$= \int_{-\infty}^{\infty} \frac{d\omega}{2\pi} \int_{-\infty}^{\infty} \frac{d^2q}{(2\pi)^2} \Gamma(\vec{q}, \omega)\, e^{-q(z_0 - z) + i\vec{q}\cdot\vec{x} - i\omega t} \quad , \quad (6.13)$$

where $$\Gamma(\vec{q}, \omega) = \frac{4\pi v_z}{v_z^2 q^2 + (\omega - \vec{v}_{\parallel}\cdot\vec{q})^2} \quad . \quad (6.14)$$

From eqs. (6.7), (6.13), the induced charge at point r, time t is obtained as

$$\rho_{ind}(\vec{r},t)=\int_{-\infty}^{\infty}\frac{d\omega}{2\pi}\int_{BZ}\frac{d^2\vec{Q}}{(2\pi)^2}\,\rho_{ind}(\vec{Q},\omega,\vec{r})e^{-i\omega t} \quad . \quad (6.15)$$

Here $\rho_{ind}(Q,\omega,r)$ takes the form

$$\rho_{ind}(\vec{Q},\omega,\vec{r})=\sum_{\substack{mn\\ d}}\left(1-\chi I\right)^{-1}_{\substack{mnd\\ m_1n_1d_1}}\chi(\vec{Q},\omega,m_1n_1d_1,d_3)$$

$$\times\left\{\sum_{G}\Gamma(\vec{Q}+\vec{G})J(\vec{Q}+\vec{G},m_1n_1d_3)\right\}\sqrt{N}\,\underline{\Phi}(\vec{Q},mnd,\vec{r}) \quad . \quad (6.16)$$

where $(1-\chi I)^{-1}$ is inverse of the matrix in the left hand side of eq. (6.7) and J(Q, m, n, d) is redefined as

$$J(\vec{Q},mnd)=\int d^3\vec{r}\;W_m(\vec{r})W_n(\vec{r}-d)e^{i\vec{Q}\cdot\vec{x}-Q(z_0-z)} \quad . \quad (6.17)$$

The energy loss of the incident electron is then evaluated from the work done by the induced field as

$$W=-\int_{-\infty}^{\infty}dt\;\mathrm{grad}\,\phi_{ind}(\vec{r},t)\Big|_{\vec{r}=\vec{r}_e(t)}\cdot\frac{d\vec{r}_e(t)}{dt} \quad . \quad (6.18)$$

Inserting $\phi_{ind}(r,t)$ calculated from $\rho_{ind}(r,t)$ in eq. (6.15) into eq. (6.18), one obtains

$$W=-\int_{0}^{\infty}\frac{d\omega}{2\pi}\int_{BZ}\frac{d^2Q}{(2\pi)^2}\,\omega\cdot\left\{\sum_{G_1G_2}\Gamma(\vec{Q}+\vec{G}_1)\Gamma(\vec{Q}+\vec{G}_2)\,\mathrm{Im}\,\Lambda(\vec{Q},\omega,\vec{G}_1,\vec{G}_2)\right\} \quad (6.19)$$

In the above, $\Lambda(Q,\omega,G_1,G_2)$ is defined as

$$\Lambda(\vec{Q},\omega,\vec{G}_1,\vec{G}_2)=\frac{1}{S}(1-\chi I)^{-1}_{\substack{m_1n_1d_1\\m_2n_2d_2}}\chi(\vec{Q},\omega,m_2n_2d_2,d_3)$$

$$\times J^{*}(\vec{Q}+\vec{G}_2,m_1n_1d_1)J(\vec{Q}+\vec{G}_1,m_2n_2d_3) \quad , \quad (6.20)$$

where S is the area of the unit cell.

The quantity

$$\sum_{G_1G_2}\Gamma(\vec{Q}+\vec{G}_1)\Gamma(\vec{Q}+\vec{G}_2)\,\mathrm{Im}\Lambda(\vec{Q},\omega,\vec{G}_1,\vec{G}_2) \quad (6.21)$$

can be thus interpreted as a loss function which gives the probability that an excitation with energy ω and with crystal momentum Q is generated in the system by an incident electron beam. Information of the elementary excitation peculiar to the system is all contained in the function $\Lambda(Q,\omega,G_1,G_2)$ and one can derive from it energy and intensity of the overlayer plasmon with a crystal momentum Q. Unless the plasmon energy is merged in the continuous energy spectrum of other excitation modes, it gives a δ-functionlike contribution to $\mathrm{Im}\Lambda(Q,\omega,G_1,G_2)$. On the other hand, if it is merged, one finds a sharp or broad peak corresponding to the plasmon in $\mathrm{Im}\Lambda(Q,\omega,G_1,G_2)$. //

B. Numerical Procedure

(1) Wannier Function

The Wannier function of the n-th band, $W_n(r)$ is calculated from the wave function $\phi_{nk}(r)$ using eq. (6.3). In the present LCAO band calculation, $\phi_{nk}(r)$ is given as

explained in section 5 by

$$\phi_{nk}(r) = \sum_{\alpha\lambda} C_{\alpha\lambda}(n,k) \sum_{l} \frac{1}{\sqrt{N}} e^{ik\cdot(l+r_\alpha)} \varphi_{\alpha\lambda}(r-l-r_\alpha) \quad . \quad (6.21)$$

From eqs. (6.3), (6.21) we find the Wannier function is also composed of linear combination of atomic orbitals,

$$W_n(r) = \sum_{\substack{\alpha\lambda \\ l}} A(\alpha\lambda, l)\, \varphi_{\alpha\lambda}(r-l-r_\alpha) \quad , \quad (6.22)$$

where

$$A(\alpha\lambda, l) = \frac{1}{N} \sum_{k} C_{\alpha\lambda}(n,k)\, e^{ik\cdot(l+r_\alpha)} \quad . \quad (6.23)$$

The coefficient $A(\alpha, \lambda, l)$ is not settled uniquely because the phase of $C_{\alpha\lambda}(n,k)$ can be freely chosen on condition that $C_{\alpha\lambda}(n,k)$ is the continuous function with respect to wavevector k. For instance, the Wannier function $W_n(r)$ undergoes displacement d if $C_{\alpha\lambda}(n,k)$ is replaced by $C'_{\alpha\lambda}(n,k) = C_{\alpha\lambda}(n,k)\exp(-ikd)$ with a lattice vector d. Therefore we must select the phase of $C_{\alpha\lambda}(n,k)$ so that $W_n(r)$ may be localized at r=0 as well as possible. We find that this is achieved fairly well by setting such a $C_{\alpha\lambda}(n,k)$ that corresponds to the dominent orbital of the n-th band to be a real positive number. The bonding-p_x, π^* and π orbital of a dimer are found to be dominent throughout the whole BZ. Therefore the coefficients $C_{\alpha\lambda}(n,k)$ corresponding to those orbitals are chosen as positive number in constructing the Wannier functions of the corresponding bands. Moreover if $C_{\alpha\lambda}(n,k)$ is chosen as described above, $C_{\alpha\lambda}(n,k)$ coincides with $C^*_{\alpha\lambda}(n,-k)$ due

to the time reversal symmetry of the system. The Wannier function then becomes a real function since

$$A^*(\alpha\lambda,\ell)=\frac{1}{N}\sum_k C^*_{\alpha\lambda}(n.k)e^{-ik\cdot(\ell+\pi_\alpha)}=\frac{1}{N}\sum_k C_{\alpha\lambda}(n.-k)e^{-ik\cdot(\ell+\pi_\alpha)}$$

$$=\frac{1}{N}\sum_{k'(=-k)} C_{\alpha\lambda}(n.k')e^{ik'\cdot(\ell+\pi_\alpha)}=A(\alpha\lambda,\ell) \quad . \quad (6.24)$$

Thus conditions of the Wannier function assumed in section 6-A is realized.

(2) Matrix Element

Here we will explain the method to evaluate matrix element I(Q,m,n,d;m',n',d') defined by eq. (6.9). Making use of the Fourier transform of the Coulomb potential, it is rewritten as

$$I(\vec{Q},mnd.m'n'd')=\frac{2\pi}{S}\sum_G\frac{1}{|\vec{Q}+\vec{G}|}\int d\pi_1 d\pi_2\, W_m(\pi_1)W_n(\pi_1-d)$$

$$\times e^{i(\vec{Q}+\vec{G})\cdot(\vec{X}_1-\vec{X}_2)-|\vec{Q}+\vec{G}||z_1-z_2|}\, W_{m'}(\pi_2)W_{n'}(\pi_2-d') \quad . \quad (6.25)$$

As each Wannier function is composed of the linear combination of atomic orbitals, we are required to calculate 4-center integrals to estimate I(Q,m,n,d;m',n',d'). But it seems almost infeasible to compute them directly using numerical atomic orbitals obtained in the band calculation. Therefore we decided to fit each numerical atomic base by the linear combination of Gaussian orbitals as follows;

$$\varphi_{\alpha\lambda}(\vec{r}) \cong \begin{pmatrix} 1 \\ x \\ y \\ z \end{pmatrix} \sum_i a_i e^{-\gamma_i r^2} \quad \text{for} \begin{pmatrix} s \\ p_x \\ p_y \\ p_z \end{pmatrix} \text{orbital} \qquad (6.26)$$

Six Gaussian orbitals are found to be sufficient to reproduce the features of the valence orbitals of Si and K almost perfectly. As the product of two Gaussian orbitals becomes a single Gaussian, the product of two Wannier functions in eq. (6.25) is expanded as

$$W_m(r)\,W_n(r-d) = \sum_{p=1}^{N} \left\{ a_p (x-u_p)^2 + b_p (x-u_p) + c_p \right\}$$

$$\times \left\{ d_p (y-v_p)^2 + e_p (y-v_p) + f_p \right\} \left\{ h_p (z-w_p)^2 + i_p (z-w_p) + j_p \right\}$$

$$\times \exp\left\{ -\gamma_p (x-u_p)^2 - \gamma_p (y-v_p)^2 - \gamma_p (z-w_p)^2 \right\} . \qquad (6.27)$$

Inserting eq. (6.27) and the similar expression for $W_{m'}(r)W_{n'}(r-d')$ into eq. (6.25), we obtain

$$I(\vec{Q}, mnd : m'n'd') = \sum_G \frac{2\pi}{S|\vec{Q}+\vec{G}|} \sum_{p\rho}^{NN'} I_1(a_p b_p c_p, u_p, \gamma_p, Q_x+G_x)$$

$$\times I_1(d_p e_p f_p, v_p, \gamma_p, Q_y+G_y)\, I_1^*(a'_\rho b'_\rho c'_\rho, u'_\rho, \gamma'_\rho, Q_x+G_x)$$

$$\times I_1^*(d'_\rho e'_\rho f'_\rho, v'_\rho, \gamma'_\rho, Q_y+G_y)\, I_2(h_p i_p j_p, w_p, \gamma_p : h'_\rho i'_\rho j'_\rho, w'_\rho, \gamma'_\rho, |\vec{Q}+\vec{G}|) \qquad (6.28)$$

Here I_1 and I_2 are defined by

$$I_1(abc, u, \gamma, Q) = \int dx \left\{ a(x-u)^2 + b(x-u) + c \right\} e^{-\gamma(x-u)^2 + iQx} \qquad (6.29)$$

$$I_2(h\,i\,j,w,\gamma:h'i'j',w',\gamma',Q)=\int dz_1 dz_2\; e^{-Q|z_1-z_2|}$$

$$\times\left\{h(z_1-w)^2+i(z_1-w)+j\right\}\left\{h'(z_2-w')^2+i'(z_2-w')+j'\right\}$$

$$\times\exp\left\{-\gamma(z_1-w)^2-\gamma'(z_2-w')^2\right\} \qquad . \quad (6.30)$$

I_1 and I_2 can be analytically integrated and one can estimate $I(Q,m,n,d;m',n',d')$ from eq. (6.28). (However, we must say its evaluation still consumes much computational time. The computational time is proportional to the 4-th power of the number of atomic orbitals which constitutes each Wannier function and furthermore we must take the summation over sufficient number of reciprocal lattices. If each Wannier function is represented by ten dominent atomic orbitals, the number of terms summed up in eq. (6.28), NN' amounts to about 10^6, which is almost the limit we are able to deal with at present stage.)

The estimation of $J(Q,m,n,d)$ defined by eq. (6.16) can be performed in the similar way. As $J(Q,m,n,d)$ includes only two center integrals, its evaluation is much easier than that of $I(Q,m,n,d;m',n',d')$.

(3) Polarization Function

The algebraic expression of the polarization function defined by eq. (6.8) consists of two terms for m>n and one for m=n. As they can be calculated in the same way, we show the method to evaluate the first term of the expression for m>n as an example. It is written in integral form as

$$\frac{1}{2\pi^2}\int_{BZ} d^2k \frac{f_{m,k-Q} - f_{n,k}}{\epsilon(m,k-Q) - \epsilon(n,k) + \omega + i\delta} e^{ik\cdot(d-d')} \quad . \quad (6.31)$$

To estimate the k-space integral, we employ a method analogous to the tetrahedron method of Lehmann et al.[34] In the method BZ is first devided into small triangles being of the same size. Then one examines the value of $f_{m,k-Q}-f_{n,k}$ in each triangle and if the boundary of two regions with different values of $f_{m,k-Q}-f_{n,k}$ crosses the triangle, it is divided into smaller ones in order that $f_{m,k-Q}-f_{n,k}$ may be constant in a triangle. In this way, the triangles are classified into three groups according as the value of $f_{m,k-Q}-f_{n,k}$ is 1 or 0 or -1. Calculation of the integral in a triangle with $f_{m,k-Q}-f_{n,k}=1,-1$ is performed by linearlizing the numerator $\exp(ik(d-d'))$ and the denominator $\varepsilon(m,k-Q)-\varepsilon(n,k)+\omega$ in it. Then The integral results in the following form

$$I_3 = \int_0^1 ds \int_0^{1-s} dt \frac{u + vs + wt}{1 + ps + qt + i\delta} \quad , \quad (6.32)$$

where we introduce new variables (s, t) in place of k. Both real and imaginary parts of I_3 can be estimated analytically and summing up the integrals in triangles, one obtains the integral (6.31).

C. Application

Let us consider the excitation modes between surface bands obtained in section 5. There appear three surface bands A, B, C near Fermi level ε_f and thus following four

kinds of excitation modes are possible; (1) B→B intraband excitation, (2) A→B interband excitation, (3) A→C interband excitation and (4) B→C interband excitation mode. Each excitation mode consists of single particle excitation and collective excitation, namely, "plasmon". The plasmon mode can exist only when polarization field due to the single particle excitation becomes large enough to make electrons oscillate collectively.

The problem is which excitation mode can be assigned to the plasmon loss peak observed by AREELS. As explained in section 4, the energy of the intra-surface-band plasmon converges to zero in the limit of Q=0. Therefore the observed plasmon may be considered as a inter-surface-band mode. For the A→C and B→C excitations, the maximum of the single particle excitation energy comes to about 3(eV). As the plasmon energy exceeds it by depolarization shift, identification of these two modes with the observed plasmon peak (1.7~1.9(eV)) seems impossible. Then only the A→B plasmon remains as a candidate for the observed one. As shown in section 5, the surface bands A,B have the character of K-4s, $4p_x$ orbitals near the G-X axis, respectively. Thus the A→B plasmon resembles the $4s-4p_x$ mode of the parallel rod model and is expected to be able to reproduce the features of the observed plasmon dispersion well. So we will calculate the dispersion of the A→B plasmon mode in the following based on the theory developed above.

For this purpose we solve the matrix equation (6.7). But in the actual calculation, the dimension of matrix, namely, the number of indices (m,n,d) incorporated in the matrix $(1-\chi I)$ must be restricted considerably because the evaluation

of matrix elements $I(Q,m,n,d;m',n',d')$ takes much computational time. As we are interested in the A→B excitation mode, it is quite physical to adopt an approximation to retain only the matrix components with $(m,n)=(A,B)$. In this approximation, the couplings with other excitation modes are neglected. In the case of the parallel rod model we find they scarcely affect the plasmon dispersions in small Q regions. So this approximation would be also adequate for the present case. In regard to the couplings with bulk excitations, we could have described them by means of "image potential" as was done in section 4. However, in the present case the effective location of the surface of substrate Si is not determined clearly because the wavefunctions of the surfacebands A,B now penetrate substrate Si layers. Furthermore it is uncertain how the image potential approximation holds true on an atomic scale. Thus we do not employ the approximation for the present case. The range of lattice vector d to be incorporated into sets of indices (m,n,d) depends on the extent of Wannier functions. As shown below, following three vectors $d=(0,0,0)$, $(0,1,0)$, $(0,-1,0)$ in units of lattice parameters are found sufficient in the present case. Then the matrix $(1-\chi I)$ in eq. (6.7) becomes 3×3.

The Wannier functions of surface bands A,B are calculated from eq. (6.22), (6.23). In order to localize them at r=0, $C_{\alpha\lambda}(n,k)$ corresponding to the bonding-p_x, π^* orbital of a dimer is chosen to be a positive real number in BZ for surface bands A,B, respectively. The composition of the obtained Wannier functions for the bands A,B is illustrated in Figs. 6.2, 6.3 for Model-1, and in Figs. 6.4, 6.5 for

Model-2. The values of $A(\alpha,\lambda,l)$ for atomic orbitals contained in the Wannier functions are listed in Tables (6.1)～(6.4) correspondingly. To make the calculation of the matrix elements practicable, 9～12 dominant atomic orbitals are incorporated into the Wannier function and the contributions of the other orbital are eliminated completely. This necessarily leads to the underestimation of the matrix elements $I(Q,.m.n.d;m',n',d')$. So we tried to retrieve it simply by multiplying the original $A(\alpha,\lambda,l)$ of the orbitals in the Wannier function by some constant that normalizes the Wannier function. For the surface band A the constant is equal to 1.14 for both Model-1 and Model-2 while for the surface band B it is equal to 1.06 for Model-1 and 1.02 for Model-2.

As can be seen from Figs. 6.2～6.5, the obtained Wannier functions of the surfacebands A,B have the same symmetry as the bonding $4p_x$, π^* orbital of a dimer, respectively. The Wannier function of the band A is even against σ_x and σ_y, whereas that of the band B is even against σ_x and odd against σ_y. Here σ_x, σ_y are mirror reflection operators which belong to the point group of the dimer site as shown in Fig. 6.7. This property results from the particular choice of the phase factor of $C_{\alpha\lambda}(n,k)$ that we employed above. Owing to this symmetry, the orthogonality between the Wannier functions of the bands A,B is satisfied automatically. Since the obtained Wannier functions are well localized along the direction perpendicular to K chains, the overlap of two Wannier functions, $W_m(r)W_n(r-d)$ becomes large only for three vectors parallel to the chains; d=(0,0,0), (0,1,0), (0,-1,0). This is the reason why

these three vectors are included in sets of indices (m,n,d). By reconstructing the Bloch functions $\phi_{nk}(r)$ from the Wannier functions, the orbital components of $\phi_{nk}(r)$ explained in section 5 can be understood more quantitatively. For instance, it is easily known that $\phi_{nk}(r)$ corresponding to the band A of Model-1 contains K-4s state dominantly along the G-X axis while K-4s is replaced by K-$4p_y$ along the Y-S axis.

As we are considering only the A→B excitation mode, the plasmon energy with a crystal momentum Q is determined directly from the condition (6.11). In the present case the matrix $(1-\chi I)$ is 3×3, but we find only one solution for eq. (6.11). In fact, it seems quite natural that there exists only one plasmon for each excitation mode. The calculated dispersion of the A→B interband plasmon of Model-1 is shown in Fig. 6.8 for the (1,-1,0) azimuth and the (1,0,0) azimuth. The shaded region indicates the maximum of the single particle excitation energy. The depolarization shift at Q=0 amounts to about 0.5(eV). The obtained plasmon dispersion exquisitely reproduces both the positive linear dispersion and the azimuth dependent anisotropy of the experimental dispersion. The slope of the dispersion at Q=0 becomes the largest for the (1,-1,0) azimuth as in the case of the parallel rod model. Moreover saturation of the plasmon energy in large Q regions, which was not reproduced by the parallel rod model that assumes free electron dispersion along the chain direction, is also realized very well. In Fig. 6.9 we showed the dispersion of the A→B interband plasmon of Model-2 for the (1,-1,0) azimuth along with the corresponding dispersion of Model-1. The shape of the

dispersion curve for Model-2 is seen almost the same as that for Model-1 and the depolarization shift at Q=0 for Model-2 also comes to about 0.5(eV). The difference of the plasmon energy between Model-1 and model-2 is attributed to the difference of the maximum single particle excitation energy that amounts to 0.4(eV) as explained in section 5.

Next, we consider the couping of the A→B excitation mode with other surface excitation modes. Especially for Model-2, the energy region of the A→B plasmon overlaps with the single particle excitation spectrum of the A→C, B→C excitation modes. Thus these modes might conceal the A→B interband plasmon from energy loss spectrum of the incident electron beam. So we solve matrix equation (6.11) taking three excitation modes (m,n)=(A,B), (A,C), (B,C) into consideration. But in this case we must be reconciled to taking only d=(0,0,0) in sets of indices (m,n,d) so as to make the calculation tractable.

The Wannier function of the surface band C is calculated by setting $C_{\alpha\lambda}(n,k)$ corresponding to the π orbital of a dimer to be a positive real number in BZ. The obtained Wannier function is illustrated in Fig.6.6 and $A(\alpha,\lambda,l)$ of each atomic orbital is listed in Table 6.5 . The Wannier function of the band C has the same symmetry as the π-orbital of a dimer and accordingly has the same symmetry as the Wannier function of the band A. Thus the orthogonality between the Wannier functions of the bands A,C is not satisfied completely on account of the numerical error and the neglect of the unimportant atomic orbitals. We simply resolved the situation by multiplying the original $A(\alpha,\lambda,l)$ corresponding to the $3p_x$-orbital of a dimer in

the Wannier function of the band C by a constant, 0.92 which makes the orthogonality between the two Wannier functions perfect.

From the imaginary part of $\Lambda(Q,\omega,G_1,G_2)$ defined by eq. (6.20), the energy loss spectrum of the electron beam is calculated. In Fig. 6.10 we showed the obtained energy loss spectrum for a crystal momentum Q=(0.11,0) (a.u.). The sharp peak at $\omega\sim1.5$(eV) corresponds to the A→B interband plasmon. Though the plasmon energy is somewhat smaller than that of Fig. 6.9, this is a numerical error caused by neglecting the matrix elements with d=(0,1,0), (0,-1,0) and has no physical meaning. The continuous loss spectrum below the A→B interband plasmon corresponds to the A→B single particle excitation spectrum, whereas that around and above it is ascribed to the A→C and the B→C single particle excitations. From the figure we can expect that the A→B interband plasmon is clearly observed in the energy loss spectrum of the electron beam even if it is merged in energy regions of other excitation modes. We find another plasmon pole at $\omega\sim4.0$(eV), which is identified as the A→C interband plasmon. As remarked above the Wannier functions of the surface bands A,C have the same symmetry and thus the matrix element I(Q,A,C,d=0;A,C,d'=0) becomes rather large. This leads the large depolarization shift of the A→C interband plasmon which comes to about 1.2(eV). On the other hand, the matrix element I(Q,B,C,d=0;B,C,d'=0) is not very large and we can not find the B→C plasmon peak in the energy loss spectrum. From these two facts, it seems reasonable to have assigned the observed plasmon peak to the A→B interband plasmon in the limits of the present

structure models. In the figure, there is an additional small loss peak near the maximum of the B→C single particle excitation energy. This peak in the B→C excitation spectrum is caused by the coupling with the A→B excitation mode, in other words, the non-diagonal matrix elements I(Q,A,B,d=0; B,C,d'=0). As the polarization field due to the A→B excitation mode is similar to that of the B→C mode, this matrix element becomes comparable with I(Q,B,C,d=0;B,C,d'=0) and gives rise to a small peak in the B→C excitation spectrum. However, we are not able to explain the physical meaning of this peak at present.

D. Summary and Discussions

Based on the band calculation in section 5, we calculated the dispersion and the intensity of the overlayer plasmons on Si(100) 2×1-K surface non-empirically. The obtained dispersion of the A→B interband plasmon is found to reproduce the observation by AREELS very well. Though we did not show the B→B intraband excitation spectrum , the energy region of this mode is smaller than those of interband modes in small Q regions. Therefore it may well be assigned to the shoulder of the observed energy loss spectrum as is done by Aruga, Tochihara and Murata.[1)]

Finally we will comment briefly on the absolute value of the A→B interband plasmon energy at Q=0. As shown in Fig.6.9, it is about 1.2(ev) for Model-1 and about 1.6(eV) for Model-2. Thus regarding the agreement with the experimental value (~1.7(eV)), Model-2 is superior to Model-1. But as we have not performed the total energy

calculations , we are not to conclude Model-2 is really preferable to Model-1 as the structure of Si(100) 2×1-K surface at present. But at least, it can be remarked that a slight change of a structure model is sufficient to shift the present plasmon energy to the experimental one. Moreover there is another problem which makes the comparison between the theory and the experiment about the plasmon energy at Q=0 difficult. That is the problem of density functional formalism on which the present band calculation is based. It is well known such band calculations underestimate small energy gaps between occupied states and unoccupied states to the order of 40%. Thus if the bandgap between the surface bands A,B is revised by some means, the plasmon energy is expected to be raised to some extent. Therefore the discrepancy between the present calculation and the experiment is not severe at all.

7. Conclusion and Discussion

Alkali overlayers form unique 1-dimensional structure on Si(100) 2×1 surface and become metallic at the full coverage. The plasmon dispersion measured in K overlayer shows the following characteristic features; (1) finite energy at Q=0, (2) positive linear dispersion and (3) azimuth dependent anisotropy, which are not explained by previous theories.

Collective modes in the array of such adatom chains are discussed in detail using the simplified rod model. It is found that the s-p_x inter-surface-band plasmon peculiar to the chain structure reproduces the features of the observed plasmon dispersion. The polarization field of this mode is vertical both to the chain direction and to the surface normal.

Detailed surface bands are obtained by the first principle band calculation. There appear three surface bands A,B,C near the Fermi level. The bands A,B,C have the K-4s, $4p_x$, $4p_z$-like character near the Γ-X line, respectively. These surface bands are found not to be influenced against the slight change of the surface structure.

The dispersions of the overlayer plasmon is calculated non-empirically based on this band calculation. The A→B inter-surface-band plasmon mode, which reproduces the observed plasmon dispersion very well, is assigned to the main loss peak of the AREELS. The subsidiary structure of the AREELS at the lower tail of the main loss peak is considered to correspond to the B→B intrasurfaceband excitation.

Next, we dicuss the validity of the assumed structure model briefly based on the present results. As explained in section 3, it is established from the LEED observation that alkali overlayers form 1-dimensional chains on Si(100) surface. The remaining problem is the determination of the adsorption site of alkali atoms. Previous experiments suggest that alkali atoms should be adsorbed on the raised site of the substrate Si and we find that such models can reproduce the observed plasmon dispersion very well. On the other hand, if alkali atoms are submerged in the substrate Si layers, the polarization fields due to the excitation between surface bands will be severely screened by bulk excitations in the substrate and it may become difficult that a surface excitation mode becomes the collective. Thus we are confirmed that alkali atoms are adsorbed on the raised site of the substrate, and probably on the raised rows of "dimers".

There still remain some interesting problems involved with the overlayer plasmon of alkali metals on Si(100) 2×1 surface which are not considered in this master thesis. One of them is the difference of the plasmon energy when K is replaced by the other alkali metals. Acoording to the experiments[26~27], the relation, $\omega_{Na} > \omega_{K} > \omega_{Cs}$, holds true. For the case of bulk metals, it is simply ascribed to the difference of the bulk electron density of these metals. But on the Si(100) 2×1 surface, the idea can not be applied because the valence electron density of alkali metals is determined by the geometry of the surface and does not depend on a kind of metals. Moreover, the energy of the overlayer plasmon, according to our interpretation,

crucially depends on the surface band structures. Therefore in order to elucidate such general trend of plasmon energy, we must calculate the electronic structures of other alkali overlayers on Si(100) 2×1 surface and must find out some characteristic features of the surface band structures common to all alkali metals.

Another interesting problem is the coverage dependence of the plasmon energy. Before the chain structure is completed, the energy loss peak due to the plasmon of the K overlayer is found to decrease gradually starting from 3~4(eV)[26~27]. At first, this energy was considered to converge to the plasmon energy corresponding to the main loss peak (1.7~2.0(eV)) at the full coverage. But very recently, Tochihara et al examined coverage dependence of the energy loss spectrum minutely and found that this energy loss might originate from another excitation mode that has the higher excitation energy than the plasmon mode responsible for the main loss peak. As this mode exists before the formation of chains, it is expected that it has a polarization field perpendicular to the surface. (It should be noted that A→B plasmon appears after the formation of chains with a considerable length.) Therefore it seems very interesting to examine the relation of this mode with the A→C plasmon mode which was found to have larger energy than the A→B plasmon.

Acknoledgements

I would like to express my sincere gratitude to Professor Masaru Tsukada for his continual guidance and encouragement throughout the course of this study. I am deeply grateful to Doctor Nobuyuki Shima for his guidance and invaluable discussions. Lastly I am willing to thank Professor H. Kamimura and all the members of the research group under Professor H. Kamimura and Professor M. Tsukada for helpful discussions and advices.

References

1) T. Aruga, H. Tochihara and Y. Murata, Phys. Rev. Lett. 53, 372 (1984)

2) J. W. Gadzuk, Phys. Rev. B1, 1267 (1970)

3) K. L. Ngai, E. N. Economou and M. H. Cohen, Phys. Rev. Lett. 24, 61 (1970)

4) H. Froitzheim, H. Ibach and D. Mills, Phys. Rev. B11, 4980 (1975)

5) W. P. Chen, Y. J. Chen and E. Burstein, Surf. Sci. 58, 263 (1976)

6) S. Ino, Jpn. J. Appl. Phys. 16, 891 (1977)

7) S. Ino and Y. Gotoh, Jpn. J. Appl. Phys. 16, 2261 (1977)

8) K. Horioka, H. Iwasaki, S. Maruno, S. T. Li and S. Nakamura Jpn. J. Appl. Phys. 16, L37 (1983)

9) T. A. Callcott and A. U. MacRae, Phys. Rev. 178, 766 (1969)

10) A. U. MacRae, K. Muller, J. J. Lander, J. Morrison and J. C. Phillips, Phys. Rev. Lett. 22, 1048 (1969)

11) S. A. Lindgren and L. Wallden, Phys. Rev. B2, 5969 (1980)

12) U. Jostell, Surf. Sci. 82, 333 (1979)

13) Tochihara

13) R. H. Ritchie, Phys. Rev. 106, 874 (1957)

14) D. M. Newns, Phys. Lett. 39A, 341 (1972)

15) R. A. Ferrel, Phys. Rev. 111, 1214 (1958)

16) R. E. Schleer and H. E. Farnworth, J. Chem. Phys. 30, 917 (1959)

17) S. Y. Tong and A. L. Maldonds, Surf. Sci. 78, 459 (1978)

18) M. J. Cardillo and G. E. Becker, Phys. Rev. Lett. 40, 1148 (1978)

19) M. Aono, Y. Hou, C. Oshima and Y. Ishijima, Phys. Rev. Lett. 49, 567(1982)

20) F. J. Himpsel and D. E. Eastmann, J. Vac. Sci. Technol. 16, 1297(1979)

21) D. J. Chadi, Phys. Rev. Lett. 43, 43(1979)

22) R. U. Rartinelli, Appl. Phys. Lett. 17, 313(1970)

23) B. Goldstein, Surf. Sci. 35, 227(1973)

24) J. D. Levine, Surf. Sci. 34, 90(1973)

25) R. Holtom and P. M. Gundry, Surf. Sci. 63, 263(1977)

26) H. Tochihara and Y. Murata, J. Phys. Soc. Jpn. 51, 2920(1982)

27) H. Tochihara, Surf. Sci. 126, 523(1983)

28) M. Tsukada, H. Ishida and N. Shima, Phys. Rev. Lett 53, 376(1984)

29) R. H. Ritchie, Phys. Lett. 38A, 189(1972)

30) F. Stern, Phys. Rev. Lett. 18, 546(1967)

31) M. Nakayama, T. Kato and K. Ohtomi, Solid State Commun. 50, 409(1984)

32) N. Shima, J. Phys. Soc. Jpn. 52, 578(1983)

33) G. S. Painter and D. E. Ellis, Phys. Rev. B1, 4747(1970)

34) G. Lehmann and M. Taut, Phys. Status Solidi 54, 469(1972)

35) J. Ihm, M. L. Cohen and D. J. Chadi, Phys. Rev. B21, 469(1972)

36) J. Harris, Solid State Commun. 16, 683(1975)

37) A. A. Lucas and M. Sunjic, Phys. Rev. Lett. 26, 29(1971)

Figure Captions

Fig. 2. 1. The box model proposed by Newns where the alkali overlayer is modeled by the uniform thin film confining free electrons.

Fig. 2. 2. Two excitation modes in Newns' model; (A) s-s intra band mode and (B) s-p_z interband mode.

Fig. 3. 1. a) The side view of Si(001) surface seen from the (1, 1, 0) azimuth before 2×1 reconstruction.
b) Symmetric dimer model.
c) Asymmetric dimer model.

Fig. 3. 2. The structure model of alkali overlayers on Si (001) surface proposed by Levine. Solid and open circles indicate alkali and Si atoms, respectively.

Fig. 3. 3. The dispersion of the overlayer plasmon measured on Si(001) 2×1-K surface by Aruga et al.

Fig. 4. 1. The parallel rod model which consists of uniform rectangular rods confining free electrons on the semi-infinite dielectric medium with a dielectric constant $\varkappa$. The axies directions are also shown.

Fig. 4. 2. Graphical derivation of the RPA equation.

Fig. 4. 3. Three coupled excitation modes in the parallel rod model; 4s-4s intraband mode (ν=1), 4s-$4p_z$ interband mode (ν=2) and 4s-$4p_x$ interband mode (ν=3).

Fig. 4. 4. Polarization field of the 4s-$4p_z$ mode. a) Q=(0. 0) , b) Q=(π/a, 0)

Fig. 4. 5. Polarization field of the 4s-$4p_x$ mode. a) Q=(0, 0) , b) Q=(π/a, 0)

Fig. 4. 6. Energy dispersion of the overlayer plasmons for the case of $\varkappa$=15, θ=45°. Solid circles show the

observed plasmon dispersion.

Fig. 5. 1. a) The side view of the thin film model KSi_8H_4 seen from the (1, 1, 0) azimuth which is common to Model-1, 2.

b) The top view of Model-1.

c) The top view of model-2.

Fig. 5. 2. Surface bands of the thin film Si_8H_4. The shaded regions are projection of bulklike bands.

Fig. 5. 3. Surface bands of the thin film KSi_8H_4. (Model-1)

Fig. 5. 4. Surface bands of the thin film KSi_8H_4. (Model-2)

Fig. 5. 5. Total density of states of the thin film KSi_8H_4 for Model-1. Three sharp peaks near ε_f correspond to surfacebands A, B, C.

Fig. 5. 6. Orbital character of the surface bands near the G -X axis.

Fig. 6. 1. Trajectory of the reflection electron beam.

Fig. 6. 2. The Wannier function of the band A for Model-1.

Fig. 6. 3. The Wannier function of the band B for Model-1.

Fig. 6. 4. The Wannier function of the band A for Model-2.

Fig. 6. 5. The Wannier function of the band B for Model-2.

Fig. 6. 6. The Wannier function of the band C for Model-2.

※ Fig. 6. 2～6. 6

a) side view seen from (1, 1, 0) direction

b) side view seen from (1, -1, 0) direction

Fig. 6. 7. Mirror reflection operators σ_x, σ_y at the dimer site.

Fig. 6. 8. The dispersion of the A→B overlayer plasmon on Si(100) 2×1-K surface for the (1, -1, 0) and the (1, 0, 0) azimuths based on the surface bands of Model-1. The shaded region indicates the maximum

of single particle excitation energy.

Fig. 6. 9. The dispersions of the A→B overlayer plasmon for the (1, −1, 0) azimuth. The plasmon energy of Model-2 exceeds that of Model-1 by ~0.4 (eV) reflecting the differense of the maximum of single particle excitation energy.

Fig. 6. 10. The energy loss spectrum of the electron beam on Si(100) 2×1-K surface. ($\mathrm{Im}\Lambda(Q, \omega, G_1=0, G_2=0)$) Three excitation modes with (m, n) = (A, B), (A, C), (B, C) are taken into consideration.

Figure 2.1

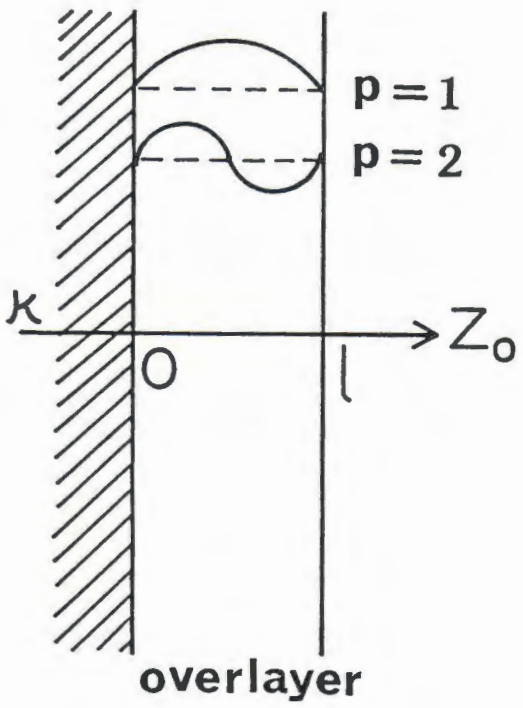

Figure 2.2

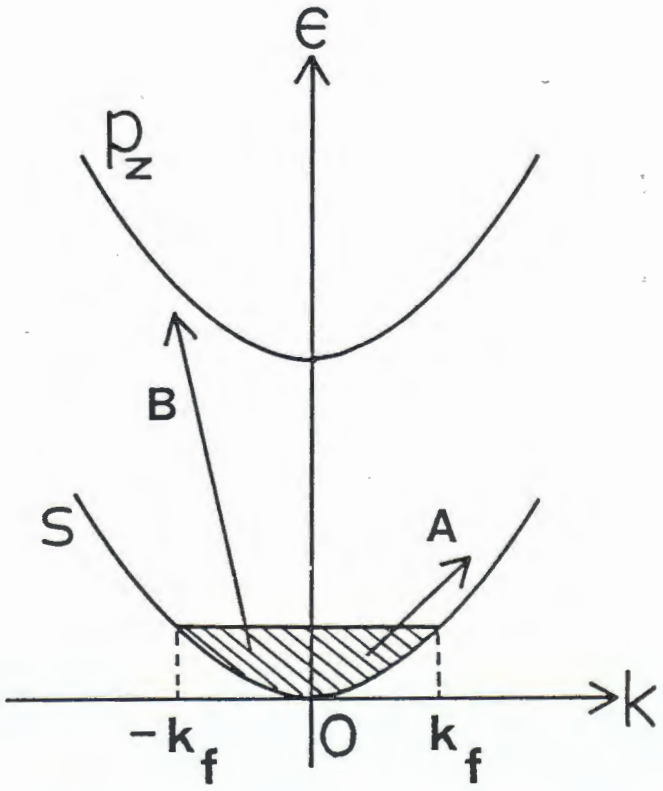

Figure 3.1

a) Si(100) surface before 2×1 reconstruction

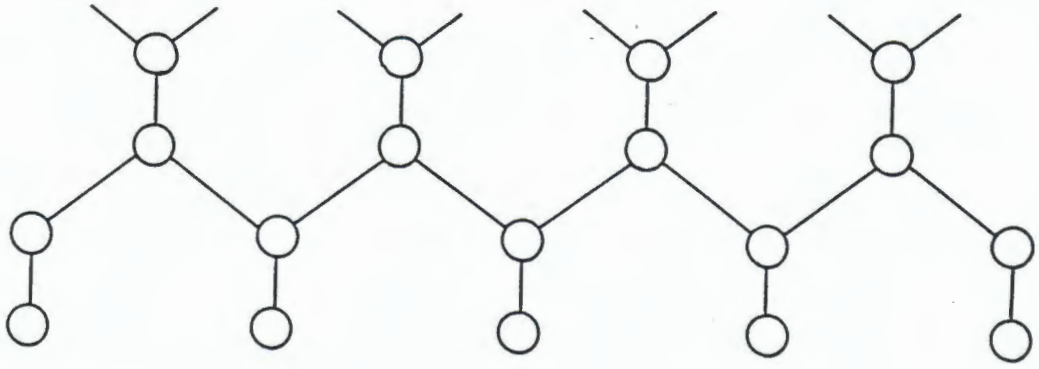

b) symmetric dimer model for Si(100) 2×1 surface

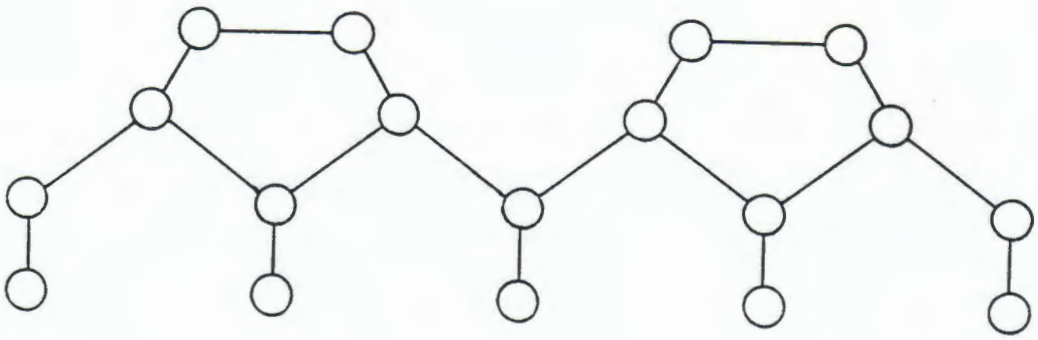

c) asymmetric dimer model for Si(100) 2×1 surface

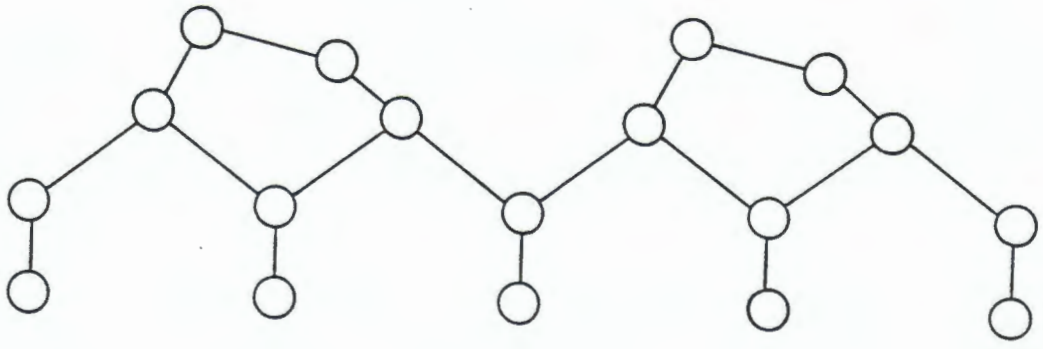

Figure 3.2

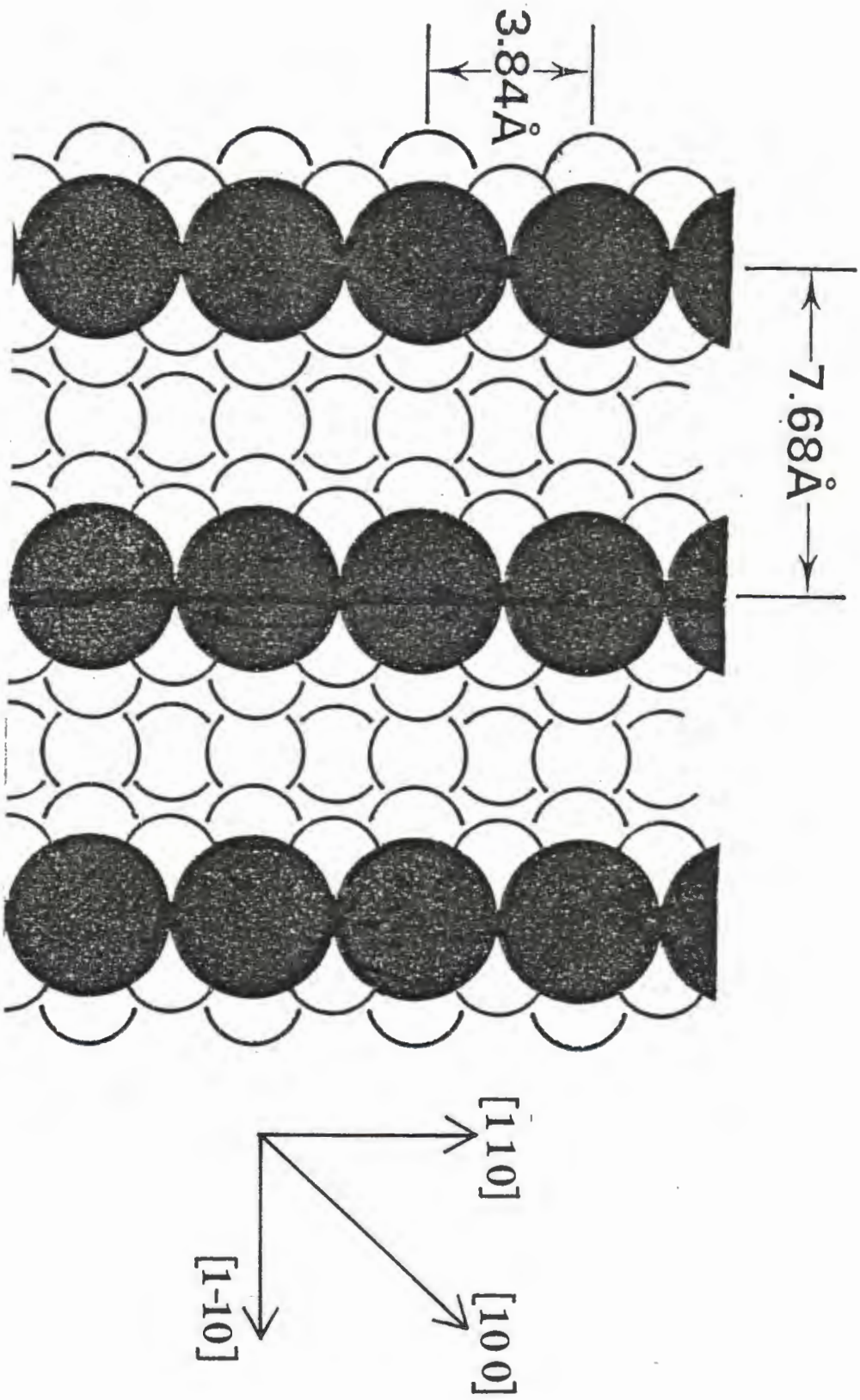

Figure 3.3

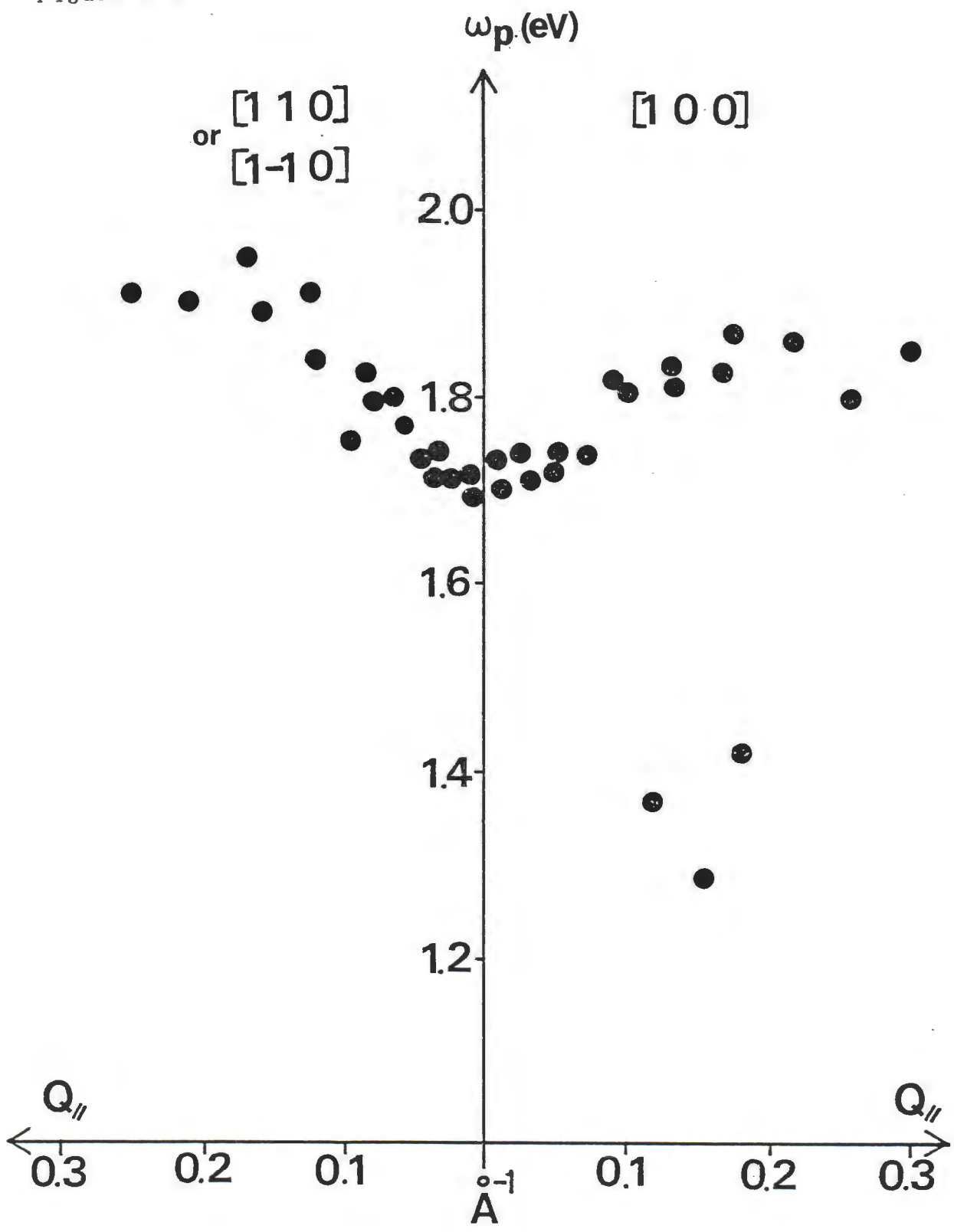

Figure 4.1

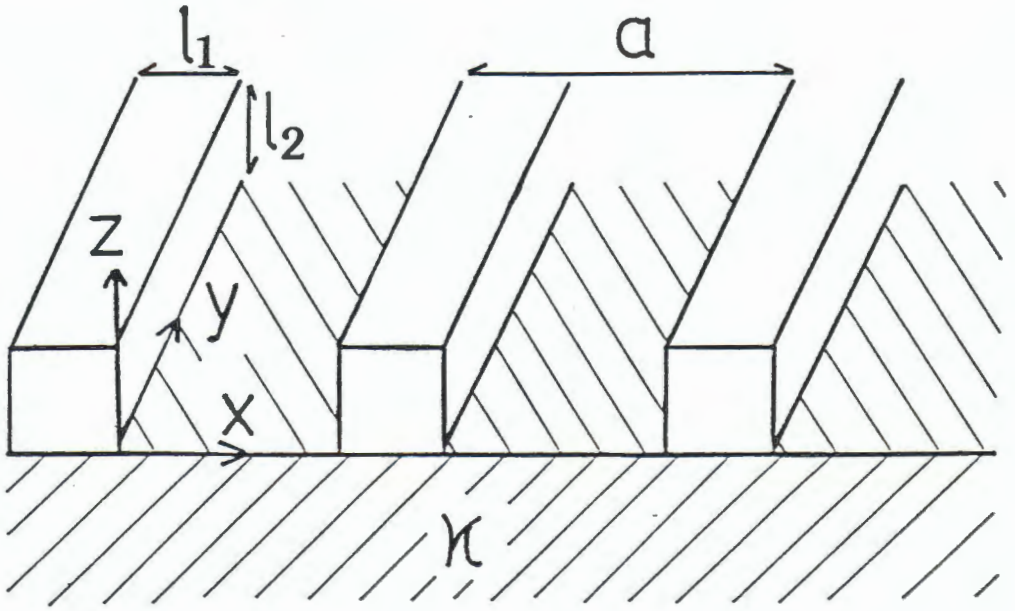

Figure 4.2

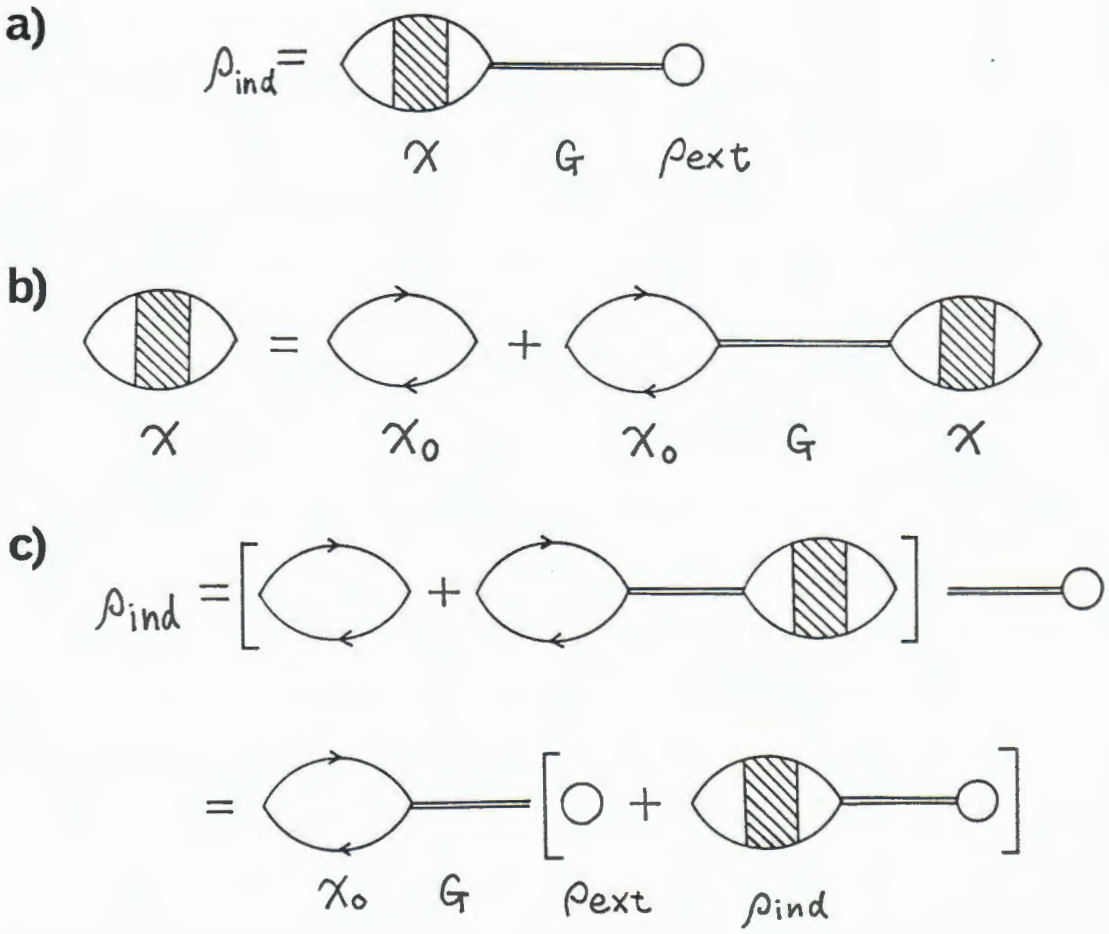

Table 4.1 Correspondence of the mode index ν and pair-band indices (p_1, p_2, q_1, q_2)

ν	Mode	p_1	p_2	q_1	q_2
1	4s-4s	1	1	1	1
2	4s-4p_z	1	1	1	2
3	4s-4p_x	1	2	1	1

Figure 4.3

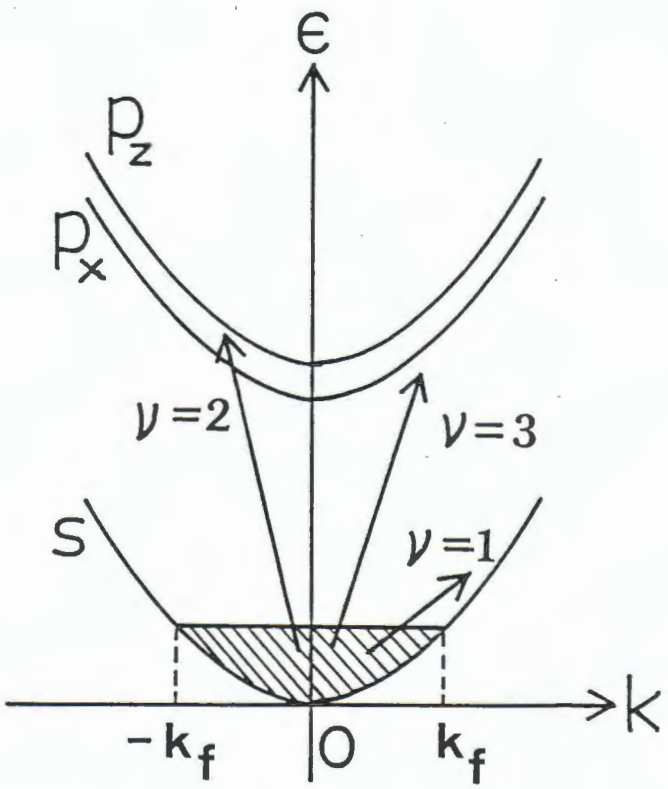

Figure 4.4

a) Q=(0.0)

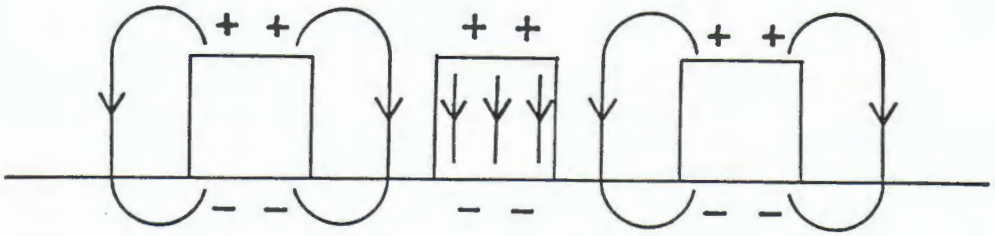

b) Q=(π/a,0)

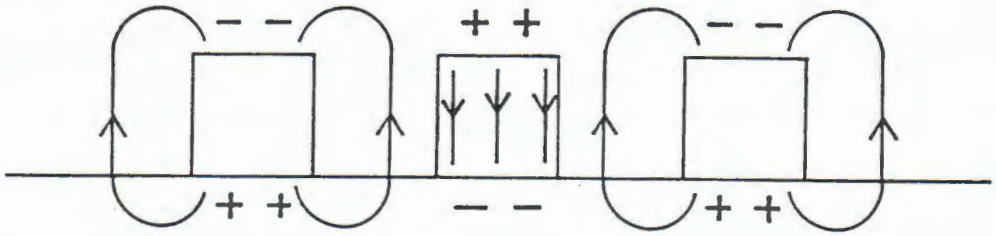

Figure 4.5

a) Q=(0,0)

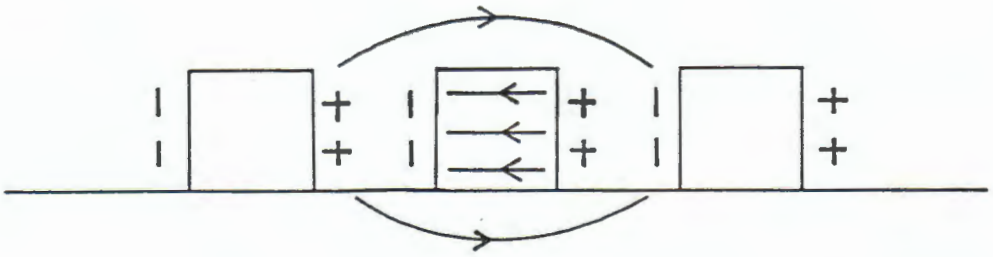

b) Q=(π/a,0)

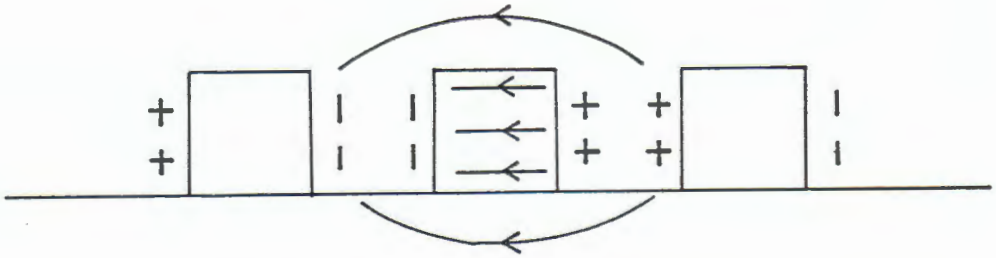

Figure 4.6

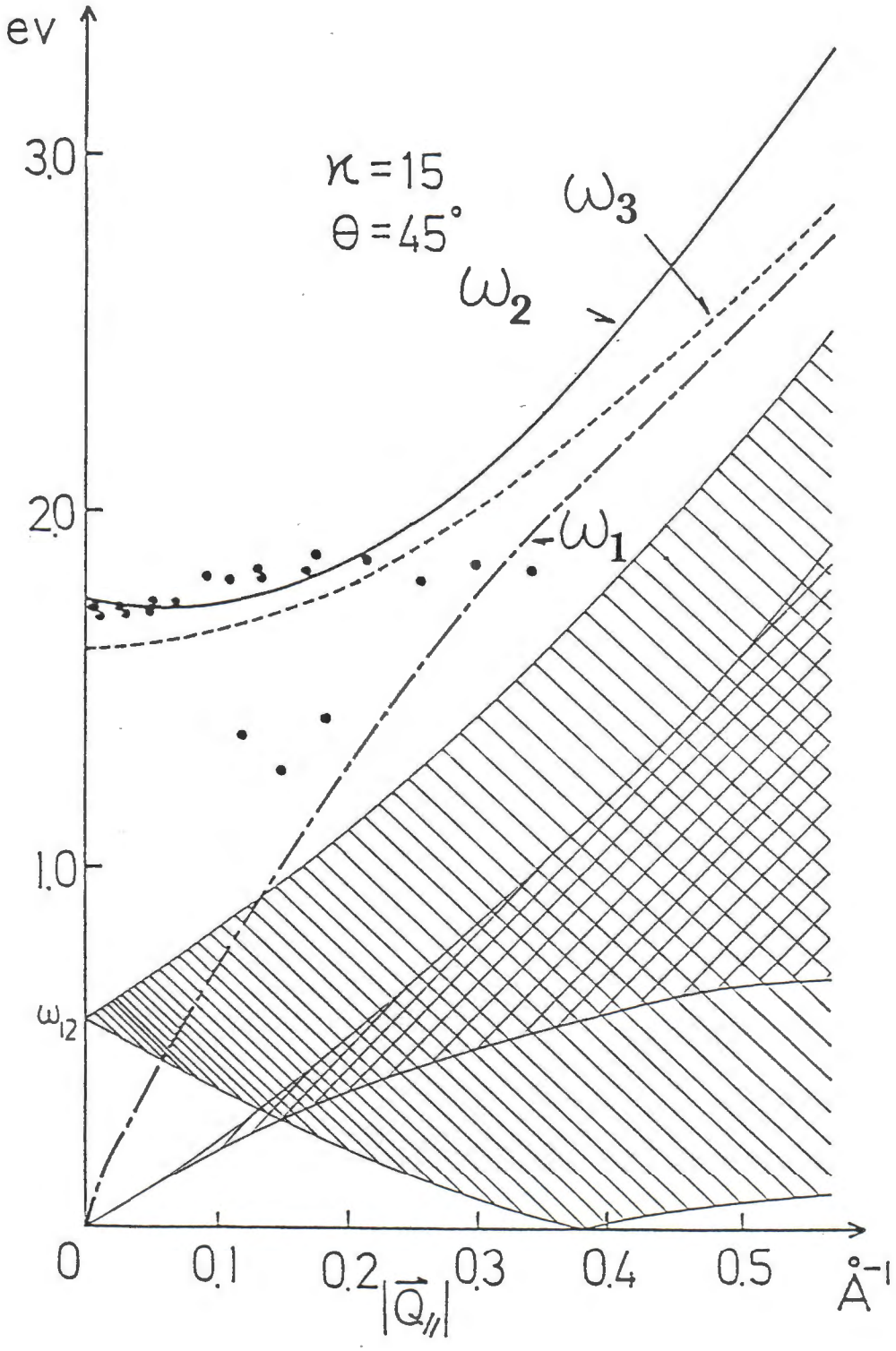
ev
3.0
2.0
1.0
ω_{12}
$\kappa = 15$
$\theta = 45°$
ω_3
ω_2
ω_1
0
0.1
0.2
0.3
0.4
0.5
Å^{-1}
$|\vec{Q}_{//}|$

Figure 5.1

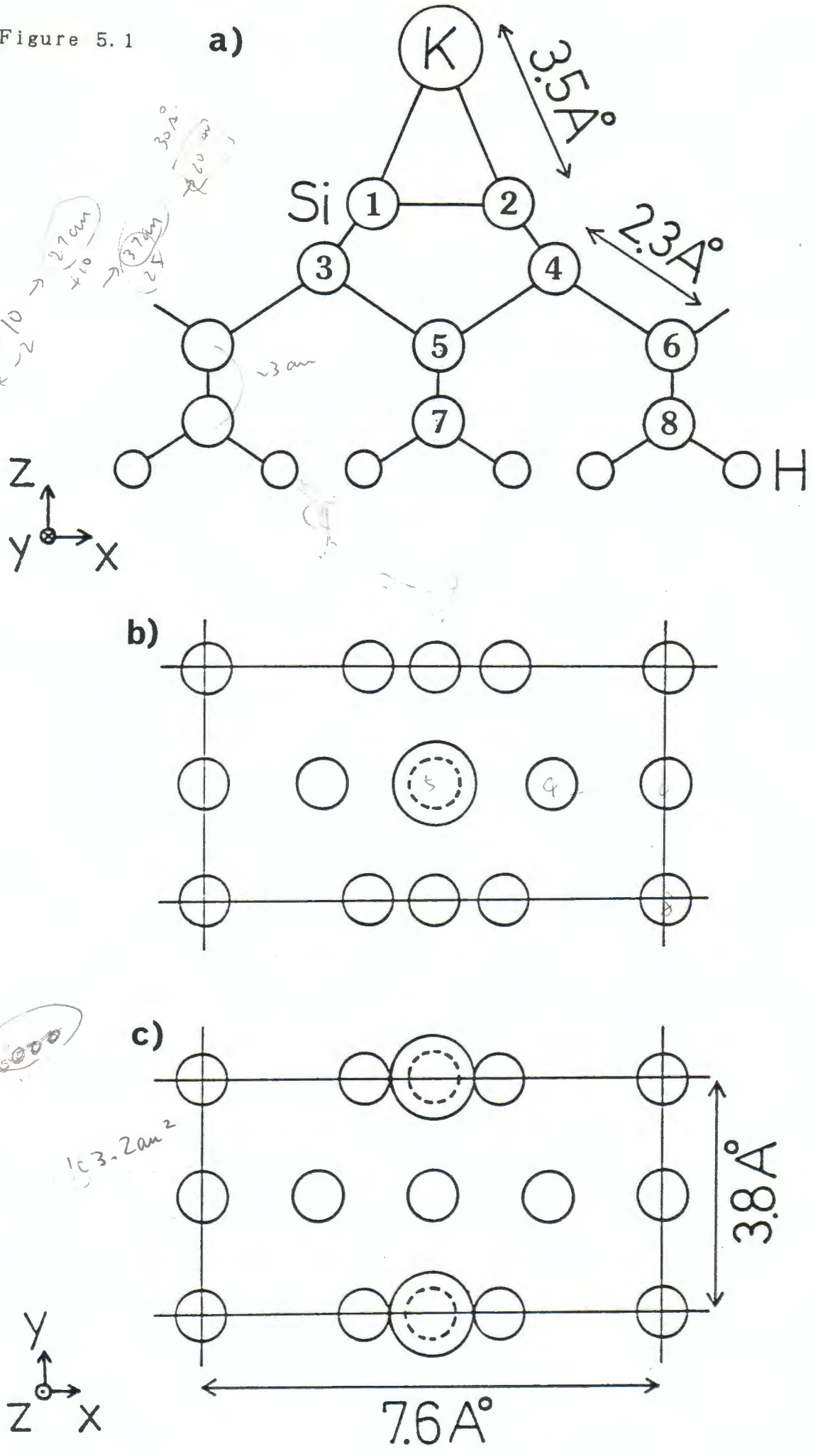

Figure 5.2

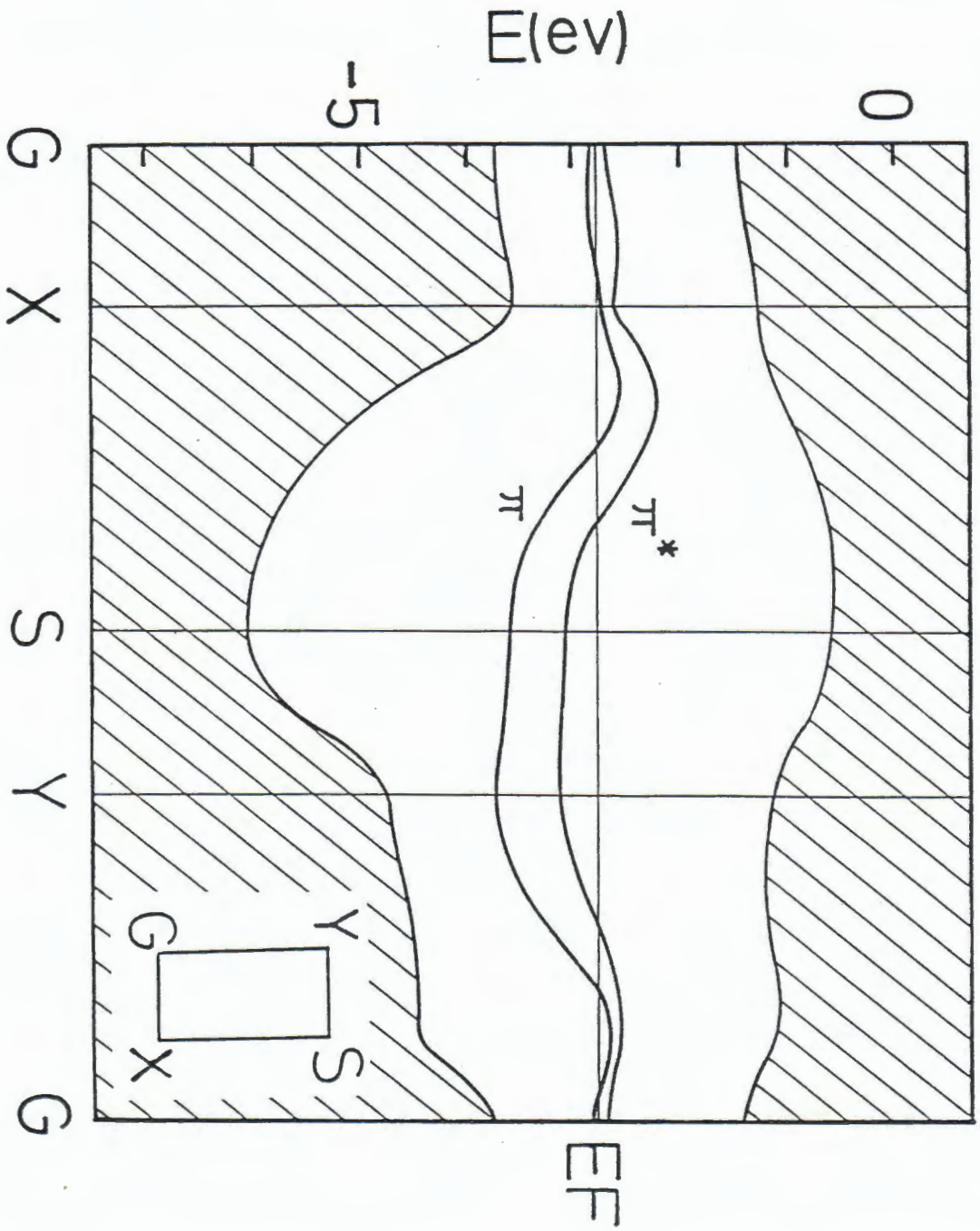

Figure 5.3

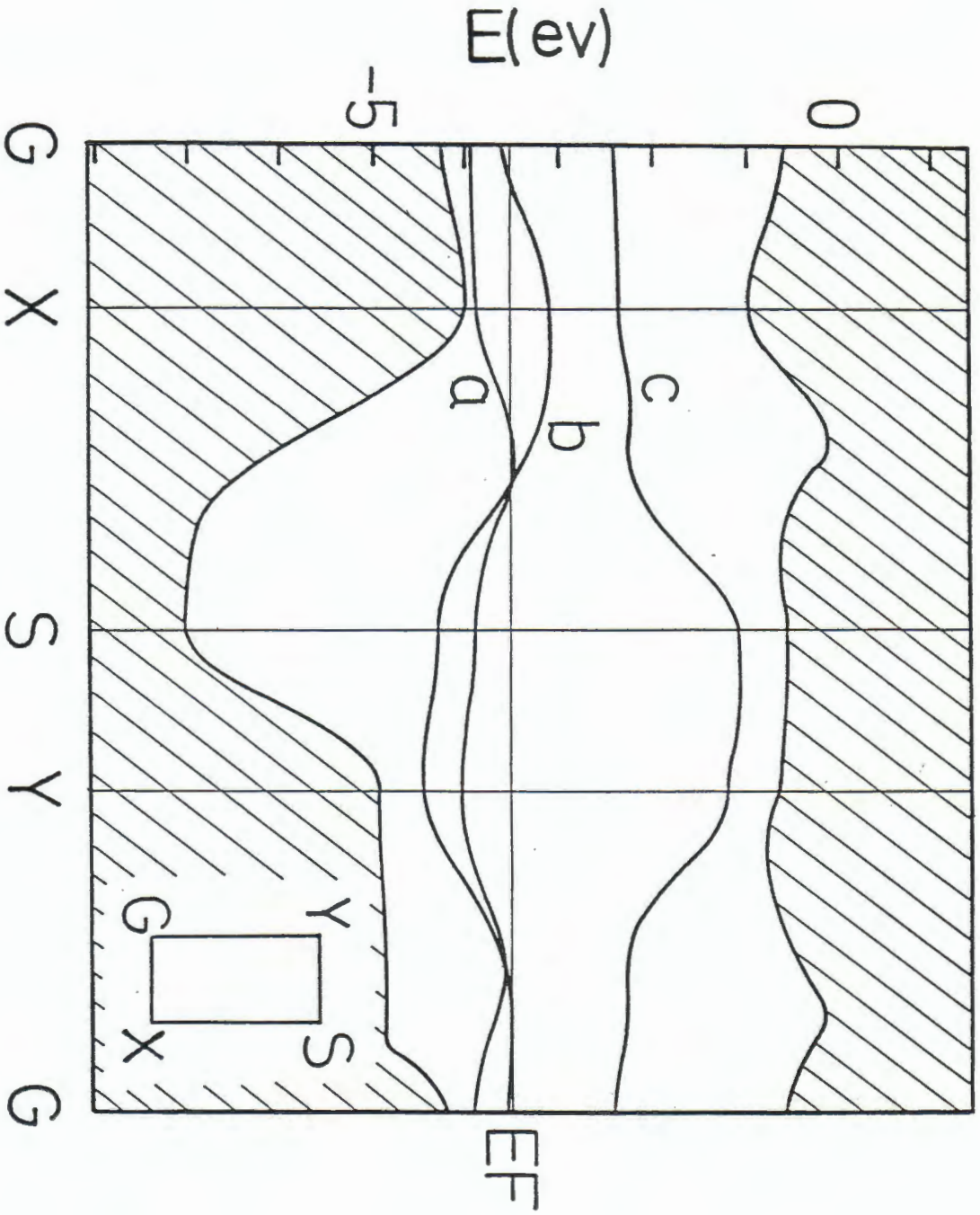

Figure 5.4

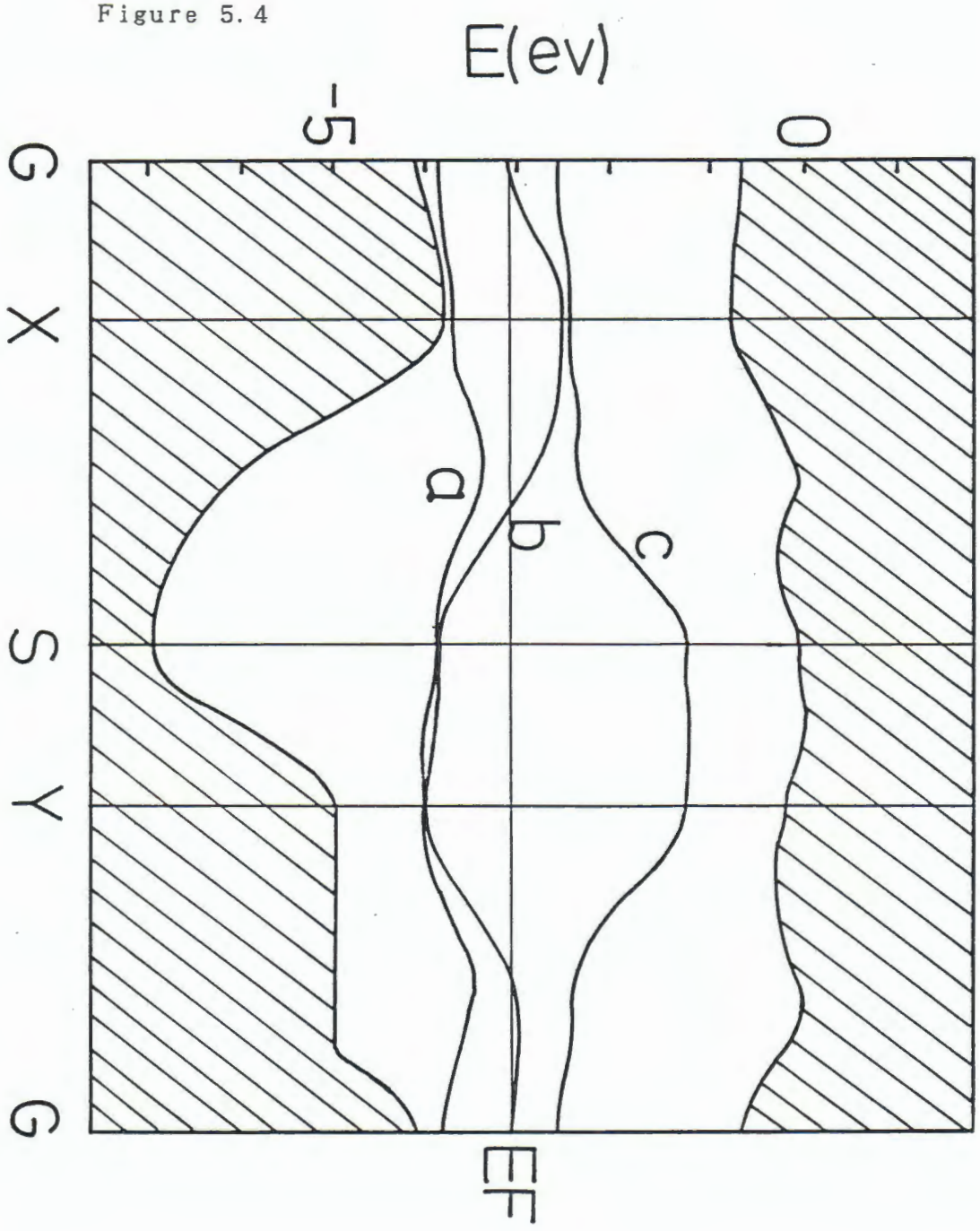

Figure 5.5

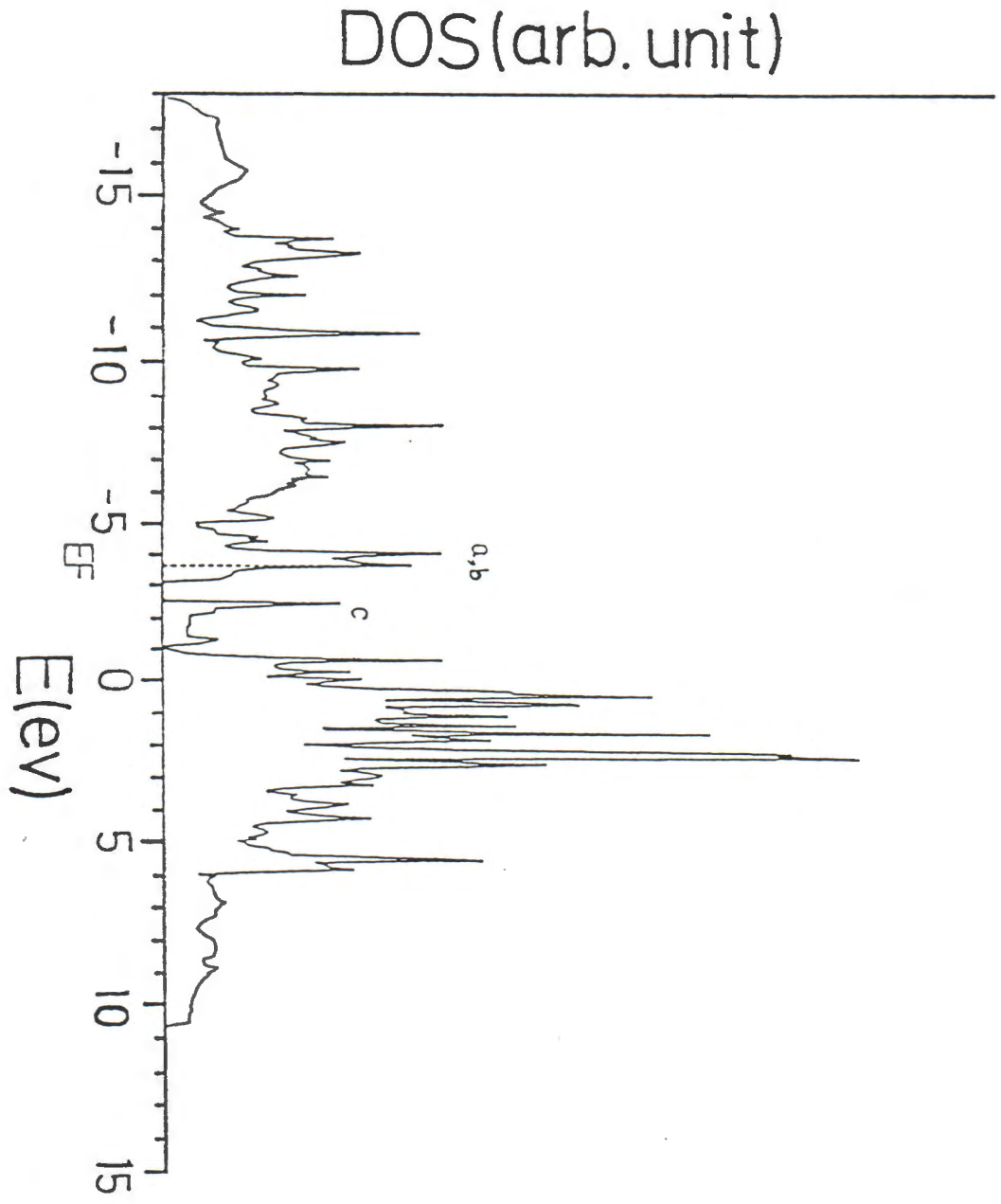

Figure 5.6

Figure 6.1

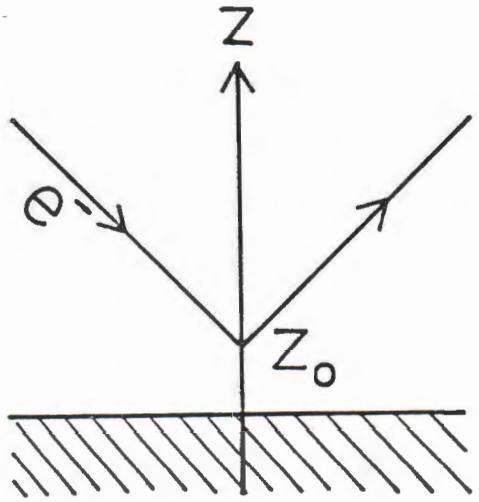

Figure 6.7

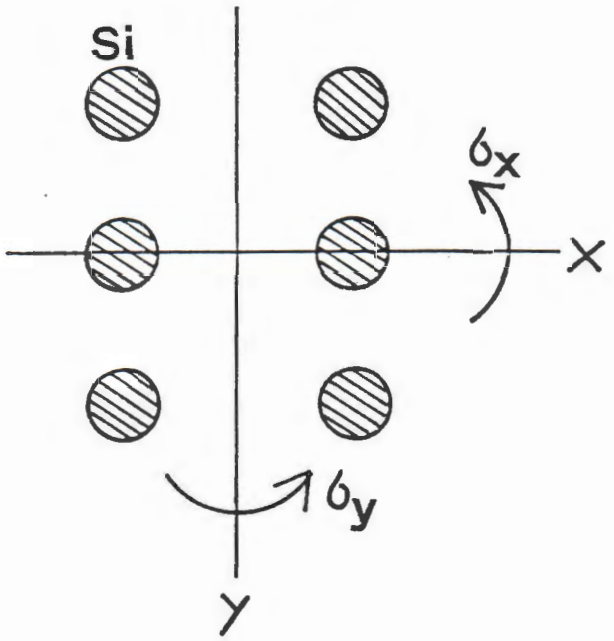

Figure 6.2 band A (Model-1)

a) b)

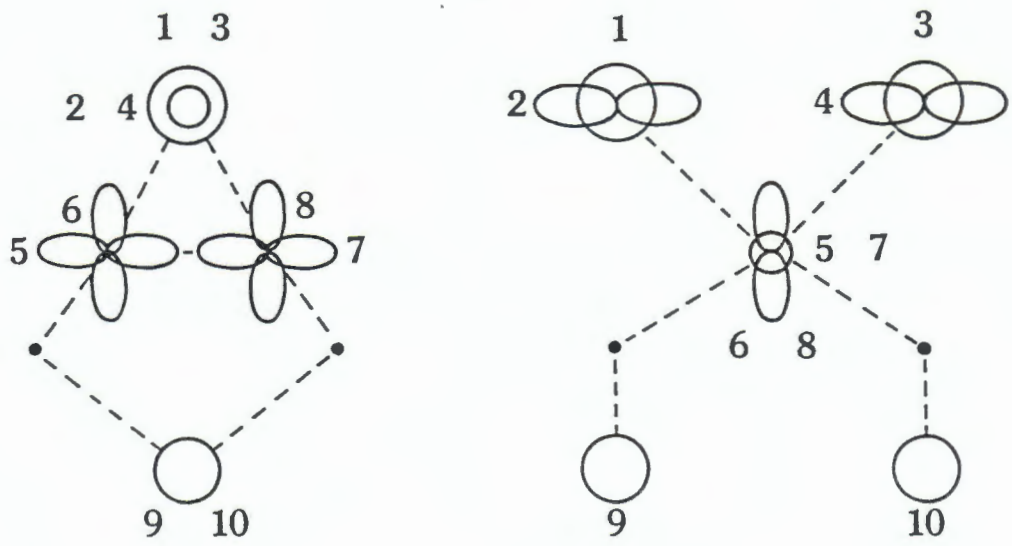

Table 6.1 band A (Model-1)

N	α	λ	l	A(α, λ, l)
1	K	4s	(0, 0, 0)	0.34
2	K	$4p_y$	(0, 0, 0)	-0.14
3	K	4s	(0, 1, 0)	0.34
4	K	$4p_y$	(0, 1, 0)	0.14
5	Si 1	$3p_x$	(0, 0, 0)	-0.40
6	Si 1	$3p_z$	(0, 0, 0)	0.25
7	Si 2	$3p_x$	(0, 0, 0)	0.40
8	Si 2	$3p_z$	(0, 0, 0)	0.25
9	Si 5	3s	(0, 0, 0)	-0.14
10	Si 5	3s	(0, 1, 0)	-0.14

Figure 6.3 band B (Model-1)

a) b)

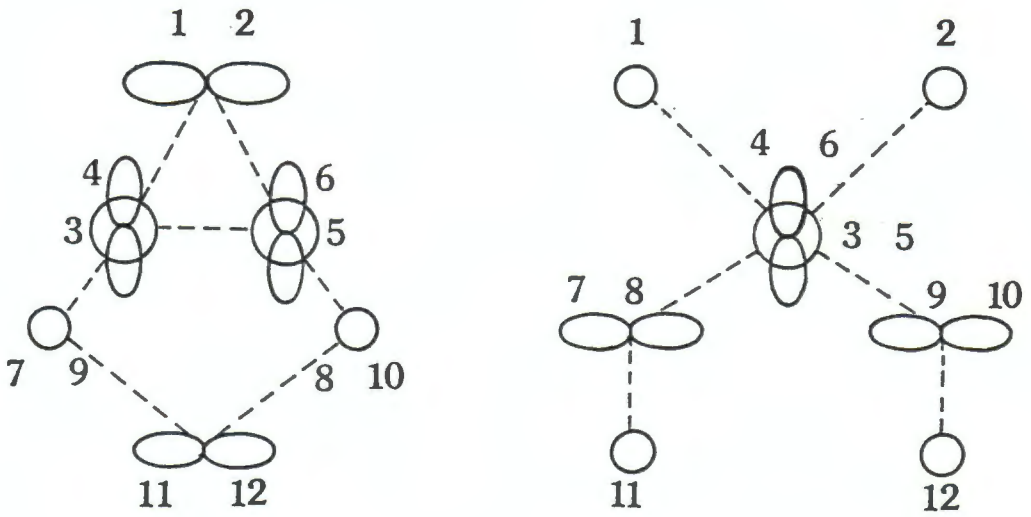

Table 6.2 band B (Model-1)

N	α	λ	l	A(α, λ, l)
1	K	$4p_x$	(0, 0, 0)	0.20
2	K	$4p_x$	(0, 1, 0)	0.20
3	Si 1	3s	(0, 0, 0)	-0.40
4	Si 1	$3p_z$	(0, 0, 0)	0.48
5	Si 2	3s	(0, 0, 0)	0.40
6	Si 2	$3p_z$	(0, 0, 0)	-0.48
7	Si 3	$3p_y$	(0, 0, 0)	-0.18
8	Si 4	$3p_y$	(0, 0, 0)	0.18
9	Si 3	$3p_y$	(0, 1, 0)	0.18
10	Si 4	$3p_y$	(0, 1, 0)	-0.18
11	Si 5	$3p_x$	(0, 0, 0)	-0.23
12	Si 5	$3p_x$	(0, 1, 0)	-0.23

Figure 6.4 band A (Model-2)

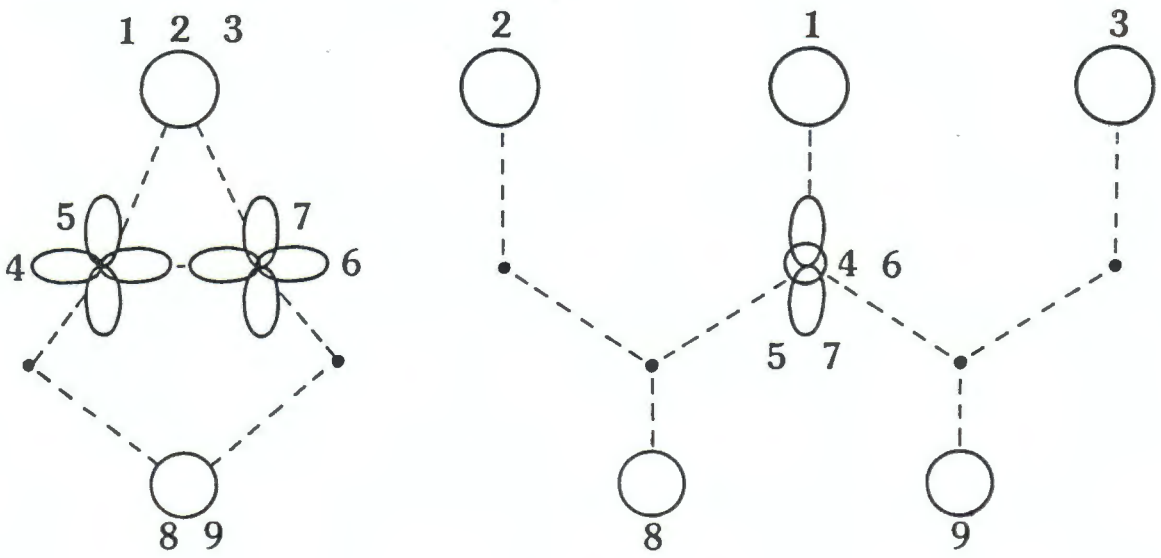

Table 6.3 band A (Model-2)

N	α	λ	l	A(α, λ, l)
1	K	4s	(0, 0, 0)	0.49
2	K	4s	(0, -1, 0)	0.16
3	K	4s	(0, 1, 0)	0.16
4	Si 1	$3p_x$	(0, 0, 0)	-0.39
5	Si 1	$3p_z$	(0, 0, 0)	0.29
6	Si 2	$3p_x$	(0, 0, 0)	0.39
7	Si 2	$3p_z$	(0, 0, 0)	0.29
8	Si 5	3s	(0, -1, 0)	-0.15
9	Si 5	3s	(0, 0, 0)	-0.15

Figure 6.5 band B (Model-2)

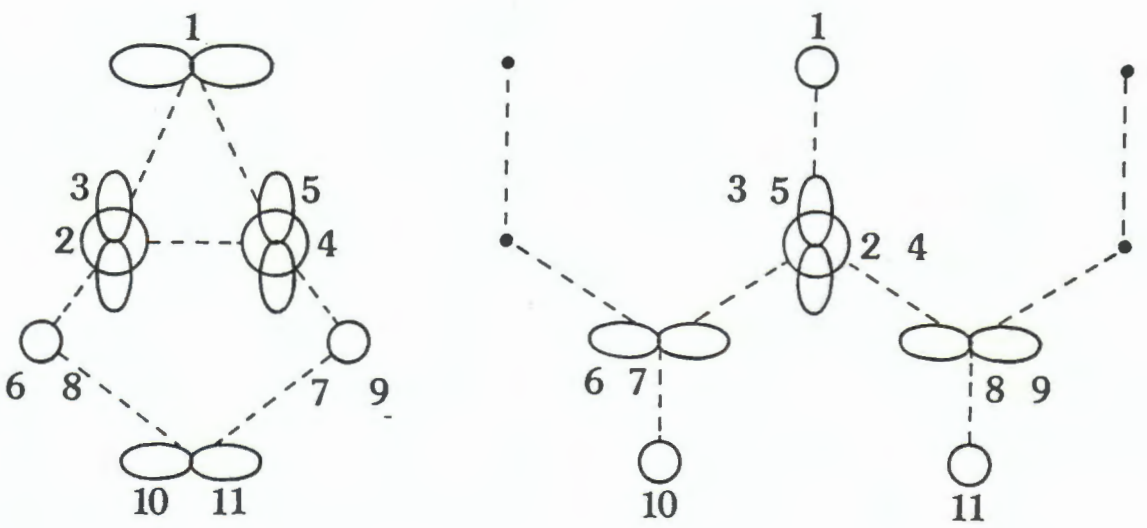

Table 6.4 band B (Model-2)

N	α	λ	l	A(α, λ, l)
1	K	$4p_x$	(0, 0, 0)	0.26
2	Si 1	3s	(0, 0, 0)	-0.40
3	Si 1	$3p_z$	(0, 0, 0)	0.45
4	Si 2	3s	(0, 0, 0)	0.40
5	Si 2	$3p_z$	(0, 0, 0)	-0.45
6	Si 3	$3p_y$	(0, -1, 0)	-0.18
7	Si 4	$3p_y$	(0, -1, 0)	0.18
8	Si 3	$3p_y$	(0, 0, 0)	0.18
9	Si 4	$3p_y$	(0, 0, 0)	-0.18
10	Si 5	$3p_x$	(0, -1, 0)	-0.24
11	Si 5	$3p_x$	(0, 0, 0)	-0.24

Figure 6.6 band C (Model-2)

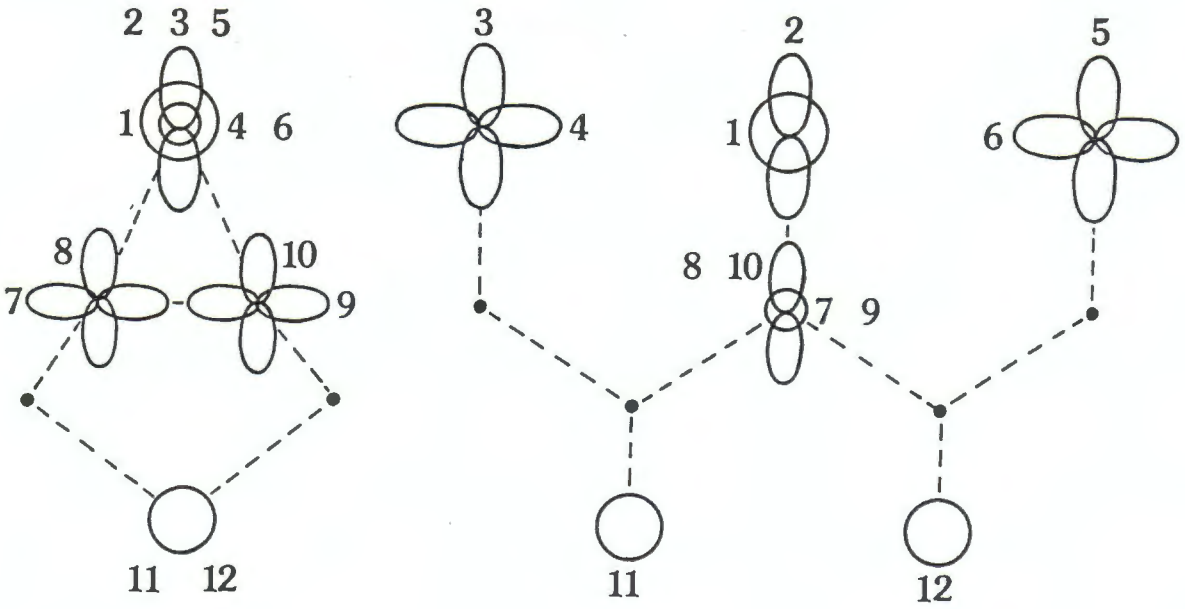

Table 6.5 band C (Model-2)

N	α	λ	l	A(α, λ, l)
1	K	4s	(0, 0, 0)	−0.50
2	K	$4p_z$	(0, 0, 0)	0.34
3	K	$4p_z$	(0, −1, 0)	0.12
4	K	$4p_y$	(0, −1, 0)	0.29
5	K	$4p_z$	(0, 1, 0)	0.12
6	K	$4p_y$	(0, 1, 0)	−0.29
7	Si 1	$3p_x$	(0, 0, 0)	−0.14
8	Si 1	$3p_z$	(0, 0, 0)	0.24
9	Si 2	$3p_x$	(0, 0, 0)	0.14
10	Si 2	$3p_z$	(0, 0, 0)	0.24
11	Si 5	3s	(0, −1, 0)	−0.16
12	Si 5	3s	(0, 0, 0)	−0.16

Figure 6.8

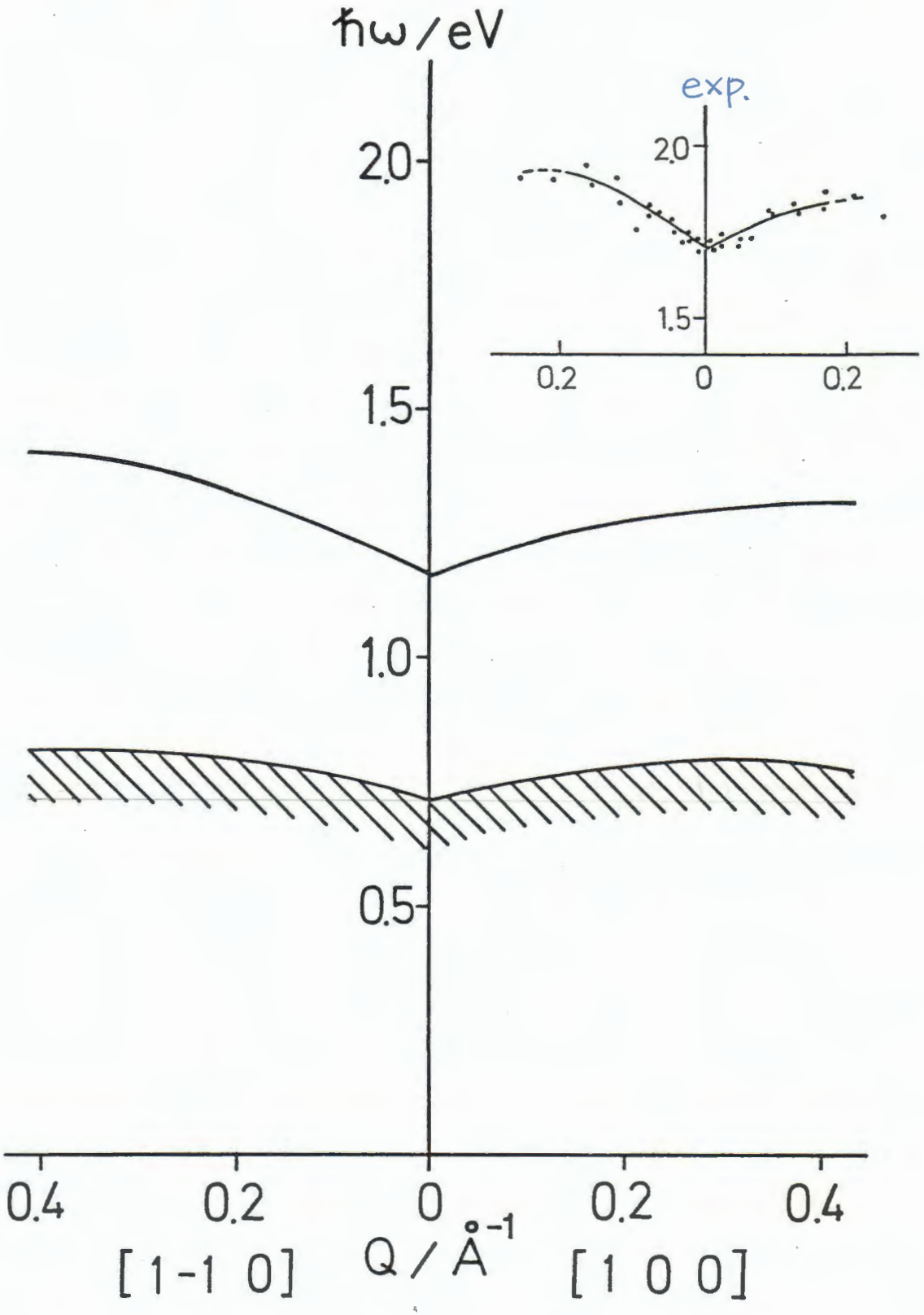

Figure 6.9

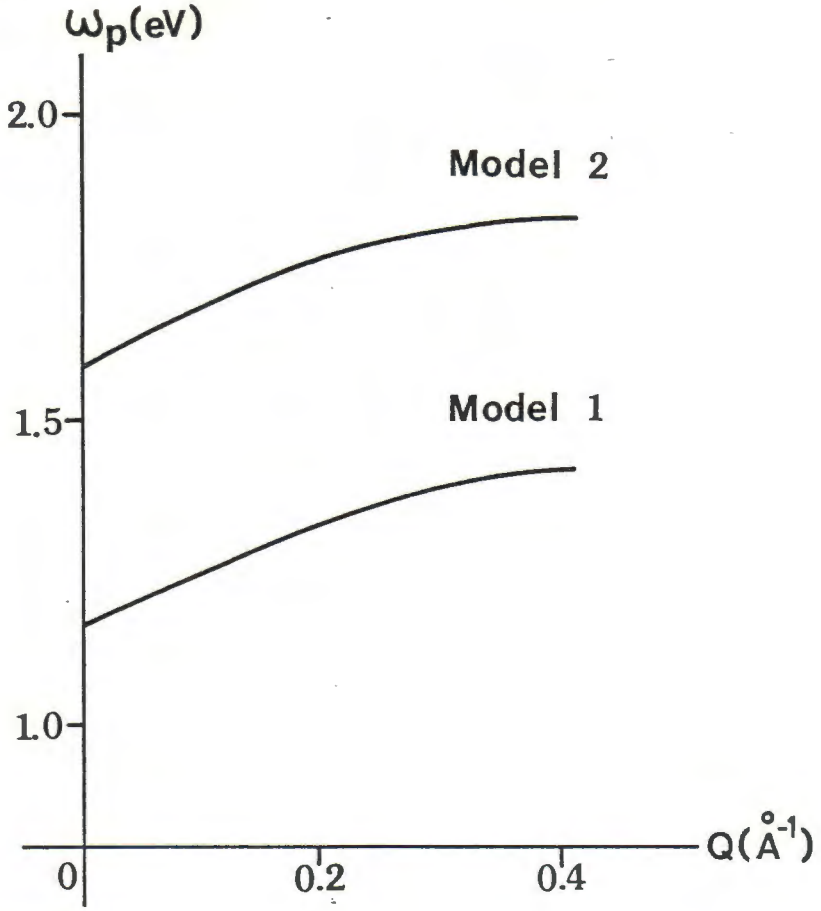

Figure 6.10

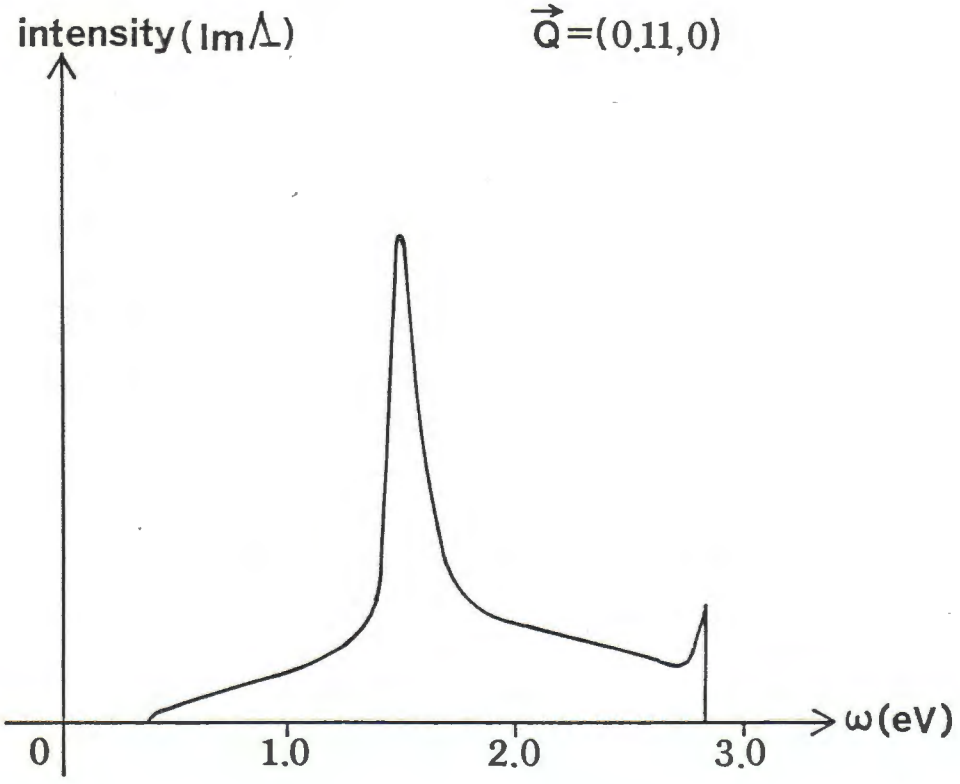

3月半ば